ROTATION PERIOD EVOLUTION IN LOW-MASS BINARY STARS: THE IMPACT OF TIDAL TORQUES AND MAGNETIC BRAKING

David P. Fleming,[1,2] Rory Barnes,[1,2] James R. A. Davenport,[1] and Rodrigo Luger[3,2]

[1] Astronomy Department, University of Washington
Box 951580, Seattle, WA 98195
[2] NASA Astrobiology Institute - Virtual Planetary Laboratory Lead Team, USA
[3] Center for Computational Astrophysics, Flatiron Institute
New York, NY 10010

ABSTRACT

We examine how tides, stellar evolution, and magnetic braking shape the rotation period (P_{rot}) evolution of low-mass stellar binaries up to orbital periods (P_{orb}) of 100 d across a wide range tidal dissipation parameters using two common equilibrium tidal models. We find that many binaries with $P_{orb} \lesssim 20$ d tidally lock, and most with $P_{orb} \lesssim 4$ d tidally lock into synchronous rotation on circularized orbits. At short P_{orb}, tidal torques produce a population of fast rotators that single-star only models of magnetic braking fail to produce. In many cases, we show that the competition between magnetic braking and tides produces a population of subsynchronous rotators that persists for Gyrs, even in short P_{orb} binaries, qualitatively reproducing the subsynchronous eclipsing binaries (EBs) discovered in the *Kepler* field by Lurie et al. (2017). Both equilibrium tidal models predict that binaries can tidally-interact out to $P_{orb} \approx 80$ d, while the Constant Phase Lag tidal model predicts that binaries can tidally lock out to $P_{orb} \approx 100$ d. Tidal torques often force the P_{rot} evolution of stellar binaries to depart from the long-term magnetic braking-driven spin down experienced by single stars, revealing that P_{rot} is not be a valid proxy for age in all cases, i.e. gyrochronology can underpredict ages by up to 300% unless one accounts for binarity. We suggest that accurate determinations of orbital eccentricties and P_{rot} can be used to discriminate between which equilibrium tidal models best describes tidal interactions in low-mass binary stars.

Keywords: binaries: close, stars: evolution, stars: kinematics and dynamics, stars: rotation

1. INTRODUCTION

The long-term angular momentum evolution of low-mass ($M \lesssim 1\,M_\odot$) stars is controlled by magnetic braking, the torque exerted on stars due to the coupling of stellar winds to the surface magnetic field (Mestel 1968). Early in stellar lifetimes, stars spin-up as they contract along the pre-main sequence. Once stars reach the main sequence, stellar radii remain mostly constant while magnetic braking removes angular momentum from the stars, gradually spinning them down over time (Skumanich 1972). Although the precise details of how magnetic braking operates are not fully known, models of magnetic braking have been used to successfully model the bulk trends of P_{rot} distributions in clusters (e.g. Praesepe, Reiners & Mohanty 2012; Matt et al. 2015; Douglas et al. 2017) and field stars (e.g. the *Kepler* field, Matt et al. 2015; van Saders et al. 2018). Furthermore, the magnetic braking-driven long-term spin-down of stars has been used to estimate stellar ages, a method known as gyrochronology (Skumanich 1972; Barnes 2003, 2007; Mamajek & Hillenbrand 2008; Barnes 2010), with older stars assumed to have lost more angular momentum due to magnetic braking and therefore rotate more slowly.

In contrast, the angular momentum evolution in low-mass short-period ($P_{orb} \lesssim 10$ d) stellar binaries is dominated by tides. Tidal torques drive secular changes in the binary orbit and stellar spins, eventually circularizing the orbit and synchronizing the stellar spins in the long-term (Counselman 1973). Orbital circularization is ubiquitous for short-period binaries, owing to the tidal torque's strong radius and semi-major axis dependence, with both theoretical (e.g. Zahn & Bouchet 1989; Claret et al. 1995) and observational (e.g. Meibom & Mathieu 2005; Mazeh 2008; Lurie et al. 2017) studies finding that most binaries with $P_{orb} \lesssim 10$ d are circularized. For short-period binaries, tidal torques work quickly on ~ 100 Myr timescales, as Zahn & Bouchet (1989) found that the orbit of solar twin binaries circularize during the stellar pre-main sequence. Observations by Meibom & Mathieu (2005) support this picture as they find short-period binaries in the ~ 150 Myr old cluster M35 tend to have circular orbits.

Tides impart a significant signature in the long-term angular momentum evolution for binary stars, especially for stellar spins. Tidal torques drive binaries towards the tidally locked state in which the stellar P_{rot} is equal to the equilibrium rotation period (P_{eq}) predicted by tidal models, with a familiar example of this effect being spin-orbit synchronization where $P_{rot} = P_{eq} = P_{orb}$. Tidal-locking occurs much earlier than orbital circularization with the tidal-locking timescale estimated to be $2-3$ orders of magnitude less than the circularization timescale (Zahn & Bouchet 1989; Witte & Savonije 2002; Mazeh 2008) as there is typically much less angular momentum in stellar spins than the binary orbit. As a result, tidal-locking is expected for binaries with $P_{orb} \lesssim 20$ d (e.g. Levato 1974; Meibom et al. 2006; Mazeh 2008; Zahn 2008; Meibom et al. 2015).

In low-mass binaries, both magnetic braking and tidal torques compete to shape the stellar P_{rot} evolution. When tides dominate, in particular at close orbital separations, tides can fix $P_{rot} = P_{orb}$, or more generally $P_{rot} = P_{eq}$ for eccentric orbits. In such situations, magnetic braking still operates, removing angular momentum from each star, forcing tides to compensate for each star's loss of angular momentum by spinning up the stars to maintain the tidally locked equilibrium, removing angular momentum from the orbit, hardening the binary (Verbunt & Zwaan 1981; Repetto & Nelemans 2014; Fleming et al. 2018). Tides do not win out over magnetic braking in general, however, as magnetic braking can spin-down the stars past the tidally locked state into subsynchronous rotation ($P_{rot} > P_{eq}$, Habets & Zwaan 1989; Zahn 1994; Keppens 1997). This behavior seems to be bourne out in nature, as Lurie et al. (2017) discovered a substantial population of subsynchronous short-period binaries in the *Kepler* field, clustered near $P_{orb}/P_{rot} \approx 0.9$, in defiance of the expectation of tidal locking at such short orbital separations. The competition between magnetic braking and tidal torques can lead to complex angular momentum evolution in low-mass stellar binaries, and no previous work has conducted a systematic study to examine how this evolution proceeds across a wide range of tidal dissipation parameters and P_{orb}.

Understanding the interaction between tidal torques and magnetic braking is of paramount importance as P_{rot} distributions measured in clusters (e.g. Praesepe, Agüeros et al. 2011; Douglas et al. 2017) and field stars (e.g. *Kepler*, Reinhold et al. 2013; McQuillan et al. 2014) are likely contaminated by unresolved binaries given that roughly half of Sun-like stars are in stellar binaries (Raghavan et al. 2010; Duchêne & Kraus 2013), and that binaries are difficult to resolve in photometric surveys. In the *Kepler* field, for example, Simonian et al. (2018) recently found that most rapid rotators ($P_{rot} \lesssim 7.5$ d) are likely non-eclipsing, tidally-synchronized short-period photometric binaries, indicating that tidal torques in binaries can significantly impact observed P_{rot} distributions. Tidally-interacting binaries impart a contaminating signal that is not currently accounted for by models. Moreover, any ages inferred from rotation periods of stars in unresolved binaries using gy-

rochronology could be incorrect owing to the influence of tidal torques. No previous study has quantified this effect.

There is currently a large number of *Kepler* binaries with known P_{rot} and P_{orb} (e.g. Lurie et al. 2017). Both the extended *Kepler* mission (K2, Howell et al. 2014) and the Transiting Exoplanet Survey Satellite (TESS, Ricker et al. 2014; Sullivan et al. 2015) are expected to detect additional low-mass eclipsing binaries, with Gaia parallaxes (Gaia Collaboration et al. 2016) poised to help refine these stellar parameters, potentially creating a rich dataset of the angular momentum budgets of low-mass binaries. Developing a framework for the angular momentum evolution of low-mass binaries can enable the characterization of the nature of tidal torques in binaries by conditioning on datasets of the spin and orbital states of stellar binaries.

Here, we present a model for the angular momentum evolution of low-mass stellar binaries over their full pre-main and main sequence lifetimes using a realistic treatment of stellar evolution, magnetic braking, and tidal torques. We investigate under what conditions tidal-locking occurs, and how tidal torques influence rotation in stellar binaries as a function of binary P_{orb} and tidal dissipation parameters for two widely-used equilibrium tidal models. We show how tidal torques can impact stellar rotation in binaries out to $P_{orb} = 100$ d, causing stellar rotation periods to not strongly correlate with age, making the predictions of gyrochronology models fail in such systems. We describe our model in § 2 and our simulation procedure in § 3. We discuss our results in § 4, apply our model to the *Kepler* field in § 4.5, and discuss our results' implications in § 5.

2. METHODS

We simulate coupled stellar-tidal evolution for low-mass binaries using an improved version of the model presented in Fleming et al. (2018). We implement our model in the open-source code VPLanet[1] (Barnes et al. 2019). We integrate all model equations (see § 2.1 and § 2.2) using the 4th order Runge-Kutta scheme with adaptive timestepping described in Fleming et al. (2018).

2.1. *Stellar Evolution*

We improve upon the interpolation of the Baraffe et al. (2015) stellar evolution models employed by Fleming et al. (2018), STELLAR, by additionally performing a bicubic interpolation of the stellar radius of gyration,

r_g, over mass and time of the Baraffe et al. (2015) models. This updated version of STELLAR now tracks the full moment of inertia evolution of low-mass stars according to the Baraffe et al. (2015) stellar evolution models, a critical requirement for modeling the angular momentum evolution of low-mass stars.

We simulate magnetic braking using the model derived by Matt et al. (2015) as this formalism has been shown to successfully model the spin-down of low-mass stars across many ages in both the Praesepe cluster and in the *Kepler* field. This model depends on the stellar Rossby number, $Ro = P_{rot}/\tau_{cz}$, the ratio of the stellar P_{rot} to the stellar convective turnover timescale, τ_{cz}. The Matt et al. (2015) model predicts that below a certain Ro for rapidly-rotating stars, stellar magnetic activity saturates at a constant value, producing a magnetic braking torque that is directly proportional to the stellar rotation rate. The angular momentum loss for rapidly-rotating saturated stars is given by

$$\frac{dJ}{dt} = -\frac{dJ}{dt}\bigg|_0 \chi^2 \left(\frac{\omega}{\omega_\odot}\right) \tag{1}$$

while for more slowly-rotating unsaturated stars,

$$\frac{dJ}{dt} = -\frac{dJ}{dt}\bigg|_0 \left(\frac{\tau_{cz}}{\tau_{cz\odot}}\right)^2 \left(\frac{\omega}{\omega_\odot}\right)^3 \tag{2}$$

where

$$\frac{dJ}{dt}\bigg|_0 = 6.3 \times 10^{30} \text{ erg } \left(\frac{R}{R_\odot}\right)^{3.1} \left(\frac{M}{M_\odot}\right)^{0.5}. \tag{3}$$

Saturated magnetic braking occurs for $Ro \leq Ro_\odot/\chi$ for $\chi = 10$ where Matt et al. (2015) defines $\chi = Ro_\odot/Ro_{sat}$. We adopt all model parameters given in Table 1 from Matt et al. (2015), with the correction from Matt et al. (2019), and compute τ_{cz} using Eqn. (36) from Cranmer & Saar (2011).

We model the net change in the stellar rotation rate due to stellar evolution and magnetic braking via the following equation

$$\dot{\omega} = \frac{\dot{J}_{mb}}{I} - \frac{2\dot{R}\omega}{R} - \frac{2\dot{r_g}\omega}{r_g} \tag{4}$$

where the moment of inertia $I = Mr_g^2R^2$, $\dot{J}_{mb}$ is the angular momentum loss due to magnetic braking, and the time derivatives of the stellar R and r_g are computed numerically using our interpolation of the Baraffe et al. (2015) stellar evolution grids.

2.1.1. *Core-Envelope Coupling*

Our simplified model assumes that stars follow solid body rotation, whereas in real low-mass stars, coupling between the radiative core and convective envelope can impact the surface rotation period evolution (MacGregor & Brenner 1991; Allain 1998; Bouvier 2008; Irwin & Bouvier 2009). Recent work by Gallet & Bouvier (2013) and Gallet & Bouvier (2015) find that the rapidly-rotating stellar core acts as an angular momentum reservoir for the convective envelope, potentially transferring angular momentum within the stellar interior and into the envelope for up to 1 Gyr, depending on the adopted magnetic braking model, the initial rotation rate, and the stellar mass. We anticipate that internal angular momentum transport would work against the spin-down caused by tidal torques, increasing tidal locking timescales. Internal angular momentum transport torques could potentially balance both tidal and magnetic braking torques near the tidally locked state, producing slight supersynchronous rotation, analogous to the subsynchronous case examined in § 4.1. Modeling core-envelope coupling is beyond the scope of this work, however.

2.1.2. *Example Stellar Evolution*

In Fig. 1, we plot the evolution of R, r_g, and P_{rot} for 0.2 $M_\odot$, 0.7 $M_\odot$, and 1 $M_\odot$ mass stars, representing an M, K , and G dwarf, respectively, computed according to STELLAR and the Matt et al. (2015) magnetic braking model. We assume all stars have an initial $P_{rot} = 1$ d and have an initial age of 5 Myr. All stars' radii contract along the pre-main sequence, spinning the stars up (right panel). Once the stars reach the main sequence, their structure changes slowly, allowing magnetic braking to dominate the stellar angular momentum evolution, significantly spinning-down the stars over long timescales. The r_g evolution noticeably differs between the stars as the late M dwarf's (green) r_g varies little as it remains fully convective, while the K and G dwarf grow a radiative core while on the pre-main sequence, decreasing r_g until both reach the main sequence.

2.2. *Tidal Evolution*

Equilibrium tidal models, first introduced by Darwin (1880), track the secular evolution of an orbiter's semimajor axis, a, eccentricity, e, and the rotation rates, ω_i, and obliquities ψ_i, of both gravitating bodies due to tidal torques. Equilibrium tidal models assume that tidally interacting bodies raise tidal bulges on their companions that remain offset from the line connecting the bodies' centers of mass due to friction within each body. This assumption is typically referred to as the "weak friction approximation" (Zahn 2008). The tidal bulges

cause torques that permit the exchange of angular momentum between the orbit and both bodies' spins. Equilibrium tidal models are linear since they assume that the tidal waves that comprise the tidal bulge raised on a body are uncoupled. Under these assumptions, the tidal evolution is analogous to a driven, damped harmonic oscillator (Greenberg 2009). For low-mass stars, equilibrium tidal models assume that tidal forces primarily dissipate energy in the outer-convective regions via viscous turbulence (see Zahn 2008). Although simple, equilibrium tidal models have been used to model the secular orbital and rotation evolution of both Solar System bodies and exoplanets (e.g. Goldreich & Soter 1966; Jackson et al. 2009; Leconte et al. 2010; Heller et al. 2011; Barnes et al. 2013; Barnes 2017) and stellar binaries (e.g. Zahn & Bouchet 1989; Zahn 2008; Khaliullin & Khaliullina 2011; Repetto & Nelemans 2014; Fleming et al. 2018). We refer the reader to Barnes (2017) for an in-depth discussion of the assumptions and limitations of equilibrium tidal models. Here, we consider two common equilibrium tidal models to study the secular spin-orbital evolution of low-mass stellar binaries.

2.2.1. *Constant Phase Lag Model*

The "Constant Phase Lag" (CPL) (Ferraz-Mello et al. 2008; Heller et al. 2011) equilibrium tidal model assumes that the tidal torque on one body due to its companion arises from a linear combination of several discrete, uncoupled tidal bulges, each with its own associated frequency, that maintain a fixed phase offset with respect to the line connecting the two stars' centers of mass. We use the EQTIDE implementation of the CPL model in VPLanet following the derivation of Ferraz-Mello et al. (2008). The equations that govern the secular change in e and a are as follows:

$$\frac{de}{dt} = -\frac{ae}{8Gm_1m_2} \sum_{i=1}^{2} Z_{i,\mathrm{CPL}} \left(2\varepsilon_{0,i} - \frac{49}{2}\varepsilon_{1,i} + \frac{1}{2}\varepsilon_{2,i} + 3\varepsilon_{5,i}\right)$$
(5)

$$\frac{da}{dt} = \sum_{i=1}^{2} \frac{da_i}{dt}$$
(6)

where if the ith body is tidally locked in a synchronous orbit,

$$\frac{da_{i,sync}}{dt} = -\frac{a^2}{Gm_1m_2} Z_{i,\mathrm{CPL}} \left(7e^2 + \sin^2(\psi_i)\right) \varepsilon_{2,i},$$
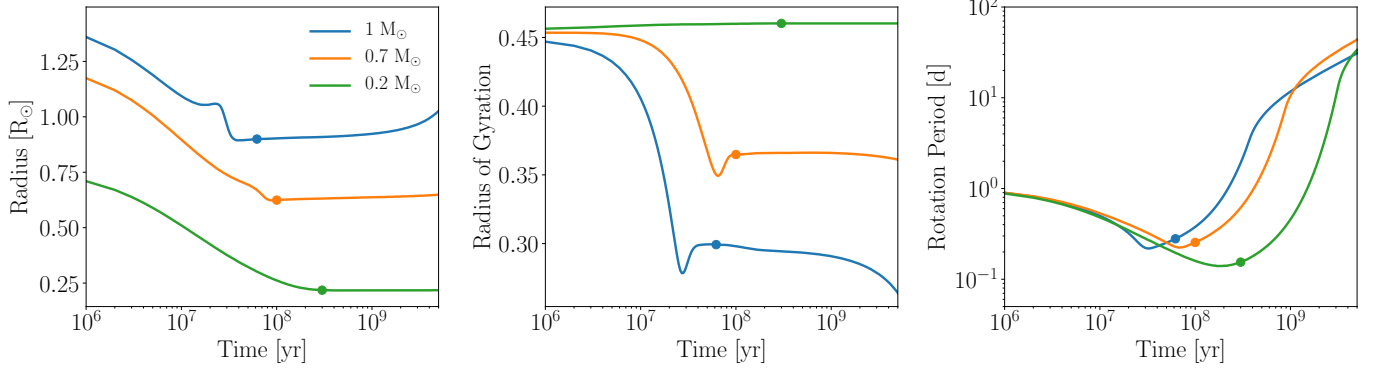(7)

Figure 1. Stellar R (left), r_g (middle), and P_{rot} (right) evolution for 0.2 $M_\odot$ (M, green), 0.7 $M_\odot$ (K, orange), and 1 $M_\odot$ (G, blue) mass stars computed according to STELLAR, our interpolation of the Baraffe et al. (2015) stellar evolution models (§ 2.1) combined with the Matt et al. (2015) magnetic braking model. Each dot denotes the approximate time when each star reaches the main sequence.

otherwise

$$\frac{da_i}{dt} = \frac{a^2}{4Gm_1m_2} Z_{i,\text{CPL}} \left(4\varepsilon_{0,i} + e^2 \left[-20\varepsilon_{0,i} + \frac{147}{2}\varepsilon_{1,i} \right. \right.$$
$$\left. \left. + \frac{1}{2}\varepsilon_{2,i} - 3\varepsilon_{5,i} \right] - 4\sin^2(\psi_i)\left[\varepsilon_{0,i} - \varepsilon_{8,i}\right] \right).$$
(8)

The CPL equations for ψ and ω evolution are

$$\frac{d\psi_i}{dt} = \frac{Z_{i,\text{CPL}}\sin(\psi_i)}{4m_i r_{g,i}^2 R_i^2 n\omega_i} \left([1-\xi_i]\varepsilon_{0,i} + [1+\xi_i](\varepsilon_{8,i} - \varepsilon_{9,i})\right)$$
(9)

$$\frac{d\omega_i}{dt} = -\frac{Z_{i,\text{CPL}}}{8m_i r_{g,i}^2 R_i^2 n}\left(4\varepsilon_{0,i} + e^2\left[-20\varepsilon_{0,i} + 49\varepsilon_{1,i} + \varepsilon_{2,i}\right]\right.$$
$$\left. + 2\sin^2(\psi_i)\left[-2\varepsilon_{0,i} + \varepsilon_{8,i} + \varepsilon_{9,i}\right]\right)$$
(10)

where G is Newton's gravitational constant, n is the binary's mean motion, and the index i denotes that i^{th} body. The tidal phase lags signs, ε, for the ith body are given by

$$\begin{aligned}
\varepsilon_{0,i} &= \Sigma(2\omega_i - 2n) \\
\varepsilon_{1,i} &= \Sigma(2\omega_i - 3n) \\
\varepsilon_{2,i} &= \Sigma(2\omega_i - n) \\
\varepsilon_{5,i} &= \Sigma(n) \\
\varepsilon_{8,i} &= \Sigma(\omega_i - 2n) \\
\varepsilon_{9,i} &= \Sigma(\omega_i)
\end{aligned}$$
(11)

where the function $\Sigma(x)$ returns 1 for positive x, -1 for negative x, and 0 otherwise.

The intermediate variable $Z_{\text{CPL},i}$ is given by

$$Z_{i,\text{CPL}} = 3G^2 k_{2,i} M_j^2 (M_i + M_j)\frac{R_i^5}{a^9}\frac{1}{nQ_i}$$
(12)

where the jth body is the ith body's companion, k_2 is the body's Love number of degree 2, and Q is the tidal quality factor ("tidal Q"). The tidal Q parameterizes the energy dissipation due to tidal evolution, with lower tidal Qs, i.e. larger phase differences between the tidal bulges, driving more rapid tidal evolution.

The other intermediate variable, ξ_i, is defined as

$$\xi_i = \frac{r_{g,i}^2 R_i^2 \omega_i a n}{GM_j}.$$
(13)

2.2.2. Constant Time Lag Model

The "Constant Time Lag" (CTL) (Hut 1981; Leconte et al. 2010) equilibrium tidal model assumes a constant time interval between the body's tidal bulge and the passage of the tidally interacting companion. In this formalism, unlike the CPL model, the CTL model is continuous over a range of tidal wave frequencies and applicable for large e. However, if the assumption of linearity is relaxed, i.e. frequencies associated with tidal bulges are allowed to depend on a spin or orbital forcing frequency, then this model is only valid over a small range of frequencies (Greenberg 2009). We use the EQTIDE implementation of the CTL model in VPLanet following the derivation of Leconte et al. (2010). The equations that govern the secular changes in e, a, ω, and ψ are as follows:

$$\frac{de}{dt} = \frac{11ae}{2GM_1M_2}\sum_{i=1}^{2} Z_{\text{CTL},i}\left(\cos(\psi_i)\frac{f_4(e)}{\beta^{10}(e)}\frac{\omega_i}{n} - \frac{18}{11}\frac{f_3(e)}{\beta^{13}(e)}\right),$$
(14)

$$\frac{da}{dt} = \frac{2a^2}{GM_1M_2}\sum_{i=1}^{2} Z_{\text{CTL},i}\left(\cos(\psi_i)\frac{f_2(e)}{\beta^{12}(e)}\frac{\omega_i}{n} - \frac{f_1(e)}{\beta^{15}(e)}\right),$$
(15)

$$\frac{d\omega_i}{dt} = \frac{Z_{\mathrm{CTL},i}}{2M_i r_{g,i}^2 R_i^2 n} \left(2\cos(\psi_i)\frac{f_2(e)}{\beta^{12}(e)} - \left[1 + \cos^2(\psi)\right]\frac{f_5(e)}{\beta^9(e)}\frac{\omega_i}{n}\right),$$
(16)

and

$$\frac{d\psi_i}{dt} = \frac{Z_{\mathrm{CTL},i}\sin(\psi_i)}{2M_i r_{g,i}^2 R_i^2 n\omega_i} \left(\left[\cos(\psi_i) - \frac{\xi_i}{\beta}\right]\frac{f_5(e)}{\beta^9(e)}\frac{\omega_i}{n} - 2\frac{f_2(e)}{\beta^{12}(e)}\right).$$
(17)

where the intermediate variables are given by

$$Z_{i,\mathrm{CTL}} = 3G^2 k_{2,i} M_j^2 (M_i + M_j)\frac{R_i^5}{a^9}\tau_i,$$
(18)

and

$$\begin{aligned}
\beta(e) &= \sqrt{1 - e^2}, \\
f_1(e) &= 1 + \tfrac{31}{2}e^2 + \tfrac{255}{8}e^4 + \tfrac{185}{16}e^6 + \tfrac{25}{64}e^8, \\
f_2(e) &= 1 + \tfrac{15}{2}e^2 + \tfrac{45}{8}e^4 + \tfrac{5}{16}e^6, \\
f_3(e) &= 1 + \tfrac{15}{4}e^2 + \tfrac{15}{8}e^4 + \tfrac{5}{64}e^6, \\
f_4(e) &= 1 + \tfrac{3}{2}e^2 + \tfrac{1}{8}e^4, \\
f_5(e) &= 1 + 3e^2 + \tfrac{3}{8}e^4.
\end{aligned}$$
(19)

In both the CPL and CTL model, We assume $k_2 = 0.5$. This choice of k_2 does not impact our results as k_2 is degenerate with Q in the CPL model, e.g. the k_2/Q scaling in Eq. (12), and with τ in the CTL model, e.g. $k_2\tau$ scaling in Eq. (18), so we instead examine how our results scale with Q and τ. Any constraints we derive as a function Q or τ can trivially be scaled to other values of k_2. For example, a common re-parameterization of Q is the reduced tidal quality factor, $Q' = 3Q/2k_2$ (e.g. Leconte et al. 2010). Given our choice of $k_2 = 0.5$, this reduces to $Q' = 3Q$.

2.2.3. Tidal Locking

Tidal torques drive a body's rotation rate towards the tidally locked state. When a body tidally locks, tidal torques fix P_{rot} to the equilibrium P_{rot}, P_{eq}. Typically, tidal locking is understood in the context of a synchronized rotator, e.g. when $P_{rot} = P_{eq} = P_{orb}$. Although spin-orbit synchronization is an expected outcome of tidal evolution (Counselman 1973), in general for tidally locked bodies on non-circular orbits, both the CPL and CTL model predict pseudosynchronous, or supersynchronous rotation, e.g. Mercury's 3:2 spin-orbit resonance ($P_{rot} = 2/3\ P_{orb}$, Goldreich & Peale 1966).

The CPL model, owing to its assumption of a finite number of discrete tidal lags, only permits a 1:1 and 3:2 spin-orbit state where, following Barnes (2017), the CPL P_{eq} is given by

$$P_{eq}^{\mathrm{CPL}} = \begin{cases} P_{orb} & \text{if } e < \sqrt{1/19} \\ \frac{2}{3}P_{orb} & \text{if } e \geq \sqrt{1/19}. \end{cases}$$
(20)

Therefore, the CPL model predicts synchronous rotation for $e \lesssim 0.23$, and a supersynchronous 3:2 spin-orbit state otherwise for tidally locked rotators.

We note that two discrete rotation states are not the only permitted ones for tidally locked systems under the CPL formalism. For example, an alternate derivation of P_{eq} for orbiters with rotation axes perpendicular to the orbital plane under the CPL model predicts

$$P_{eq} = \frac{P_{orb}}{1 + 9.5e^2},$$
(21)

a continuous function of e (Goldreich 1966; Murray & Dermott 1999). Here, we follow the suggestions of both Barnes et al. (2013) and Barnes (2017) and use the discrete P_{eq} version of the CPL model for self-consistency.

The CTL model is continuous over a range of tidal frequencies and therefore predicts a P_{eq} that is a continuous function of both e and ψ. Following Barnes (2017), we define the CTL P_{eq} by

$$P_{eq}^{\mathrm{CTL}} = P_{orb}\frac{\beta^3 f_5(e)(1 + \cos^2(\psi))}{2f_2(e)\cos(\psi)}.$$
(22)

The CTL model predicts that bodies on eccentric orbits tidally lock into supersyncronous rotation, and only bodies with aligned spins on circular orbits are synchronous rotators.

In general, a continuous P_{eq} and the discrete 1:1 and 3:2 spin-orbit commensurabilities are not the only equilibrium rotation states for tidally locked rotators predicted by equilibrium tidal models. For example, Rodríguez et al. (2012) show that tidally interacting bodies can get captured into many spin-orbit resonances states, e.g. 2:1, 5:2, 4:3, etc, and below, we search for evidence of them in data of the spin-orbital states of Kepler EBs. Note that our model does not resolve capture into such states as the CPL model, owing to its inclusion of only 4 discrete tidal lags, only allows a body to enter into 3:2 and 1:1 spin - orbit commensurabilities. The CTL model predicts a continuous equilibrium period as a function of the P_{orb}, e, and obliquity, for tidally locked bodies, only resolving capture into 1:1 synchronous rotation.

2.2.4. Numerical Details of Tidal Locking

Due to the discontinuities in the equilibrium tidal model equations, for example in Eq. (11) when $\omega \approx n$, and due to the inherant discreteness of numerical integrations, numerical solutions for the CPL and CTL models can produce unphysical evolution. We follow Barnes et al. (2013) and Fleming et al. (2018) and fix $P_{rot} = P_{eq}$ according to Eq. (20) or Eq. (22) for the CPL and CTL models, respectively, when P_{rot} is within

1% of P_{eq}. To ensure that tidal torques dominate over torques due to magnetic braking and stellar evolution when forcing tidal-locking, we additionally require that the P_{rot} derivative points towards P_{eq} on both sides of P_{eq}, i.e. when the gradient of P_{rot} points towards the tidally locked state, before fixing $P_{rot} = P_{eq}$. We find that this scheme produces physically and numerically accurate results.

2.2.5. *The Dynamical Tide*

An additional mechanism for tidal dissipation in low-mass stellar binaries is the dynamical tide. This effect arises from the turbulent viscous damping of inertial waves that are excited in the stellar convective envelope by a tidal perturber, with Coriolis acceleration serving as the restoring force (Zahn 1975; Ogilvie & Lin 2007). Under the dynamical tide formalism, the stellar mass, evolving stellar structure, rotation rate, and tidal forcing frequency can all strongly impact the strength of tidal dissipation, which can span many orders of magnitude (Ogilvie & Lin 2007; Ogilvie 2013; Mathis 2015; Gallet et al. 2017). For example, adopting the tidal frequency-averaged model for tidal dissipation of Ogilvie (2013), both Mathis (2015) and Gallet et al. (2017) show that dynamical tidal dissipation is enhanced during the pre-main sequence due to the expansion of the stellar radiative core and rapid rotation, whereas the magnetic braking-driven spin-down on the main sequence decreases the tidal dissipation. Dissipation due to the dynamical tide could be important for some of the systems considered in this work since, for binary stars on circular orbits, inertial waves are excited in the stellar convective envelopes for $P_{orb} > P_{rot}/2$ and can drive significant spin and orbital evolution (e.g. Witte & Savonije 2002; Ogilvie & Lin 2007; Bolmont & Mathis 2016). Although semi-analytic models for dynamical tidal dissipation that account for the evolving stellar structure and rotation exist (e.g. Mathis 2015; Bolmont & Mathis 2016; Gallet et al. 2017), we do not consider them here as they are currently limited to circular orbits. We instead focus on exploring the impact of the equilibrium tide across a wide range of parameter space and leave an examination of how the combination of the dynamical and equilibrium tide impacts the rotation period evolution of low-mass binary stars for future work.

2.2.6. *Example Tidal Evolution*

We plot the tidal evolution for a, e, and P_{rot}, ignoring stellar evolution, for a solar-twin binary with an initial $P_{orb} = 10$ d, $P_{rot} = 1$ d, $e = 0.2$ for the CPL model and CTL model, assuming $Q = 10^6$ and $\tau = 0.1$ seconds,

respectively, in Fig. 2. The CPL and CTL model predict the same qualitative evolution: both the binary's e and P_{orb} slightly increase as tides force the spins toward the tidally locked state, transferring rotational angular momentum into the orbit, increasing the orbital angular momentum by $\sim1\%$ in the process. At late times, both the CPL and CTL drive the binaries towards orbital circularization, with tidal dissipation decreasing P_{orb}. The predictions of the CPL and CTL model, differ, however, when the binaries tidally lock. Under the CPL model, the binary tidally locks into a synchronous orbit when $e < \sqrt{1/19}$, e.g. Eq. (20), while the CTL model predicts supersyncronous rotation due to the CTL model's equilibrium period eccentricity dependence, e.g. Eq. (22).

2.3. *Coupled Stellar-Tidal Evolution For tidally locked Systems*

Following Fleming et al. (2018), when one or both binary stars are tidally locked, tidal forces prevent magnetic braking from spinning down the tidally locked star(s), and any angular momentum lost comes at the expense of the binary orbit, decreasing a as a result (Verbunt & Zwaan 1981). Below in Eq. (23) and Eq. (24), we modify the a decay equations due to stellar evolution and magnetic braking in tidally locked binaries from Fleming et al. (2018), their Eqs. (18) and (20), to additionally account for r_g evolution when one or both stars tidally lock, respectively, assuming conservation of angular momentum:

$$\dot{a}_{coupled}^{(1)} = \frac{-\dot{J}_{mb} - 2\omega\left(m_1 r_{g,1}^2 R_1 \dot{R}_1 - m_1 r_{g,1} \dot{r}_{g,1} R_1^2\right)}{\frac{\mu^2 GM(1-e^2)}{2J_{orb}} - \frac{3\omega}{2a} m_1 r_{g,1}^2 R_1^2} \quad (23)$$

and

$$\dot{a}_{coupled}^{(2)} = \frac{-\dot{J}_{mb} - 2\omega\left(\sum_{i=1}^{2} m_i r_{g,i}^2 R_i \dot{R}_i + m_i r_{g,i} \dot{r}_{g,i} R_i^2\right)}{\frac{\mu^2 GM(1-e^2)}{2J_{orb}} - \frac{3\omega}{2a}\left(m_1 r_{g,1}^2 R_1^2 + m_2 r_{g,2}^2 R_2^2\right)}, \quad (24)$$

where J_{orb} is the orbital angular momentum.

3. SIMULATIONS

We examine stellar angular momentum evolution in low-mass binaries by simulating two sets of 10,000 stellar binaries, one modeled using the CPL model and the other using the CTL formalism. We simulate both stars' spin evolution but mainly consider the P_{rot} evolution for the primary, i.e. more massive star in binaries, as it is observationally easier to measure a P_{rot} on the more massive, and hence brighter, star (e.g. Meibom et al. 2006; Lurie et al. 2017). For each simulation, we sample the primary's mass uniformly over $[0.1, 1]$ $M_\odot$. Following Matt et al. (2015), we uniformly sample the $\log_{10}$ of P_{rot} over $[0.8, 15]$ days, a distribution that approximates the P_{rot} distribution of young stars in the ~2 Myr
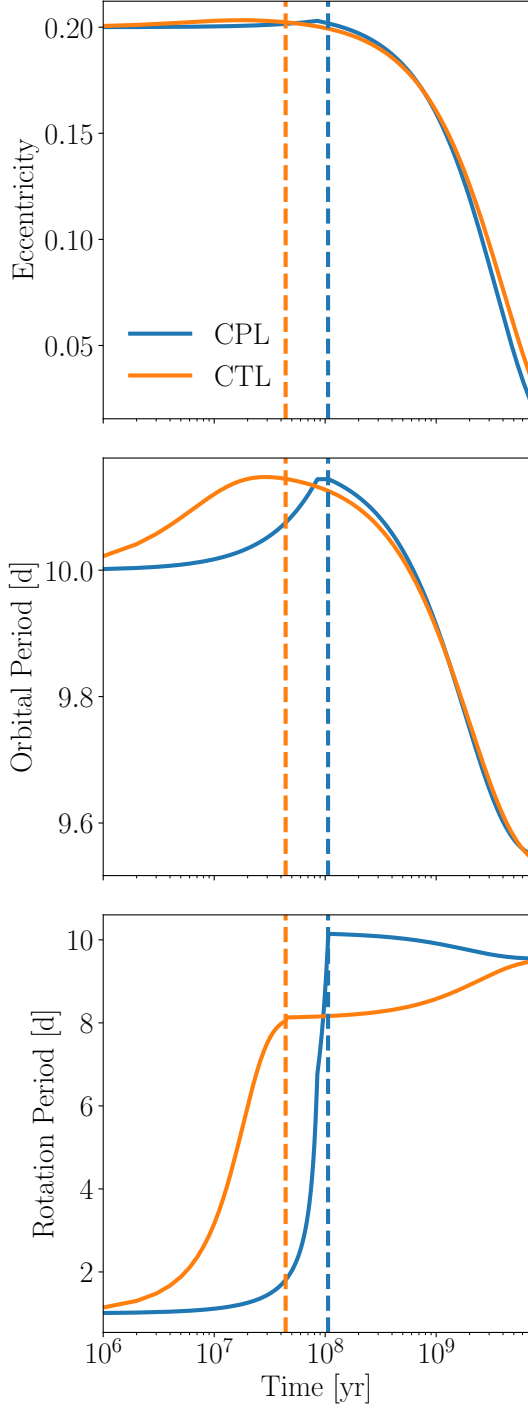
Figure 2. Tidal evolution of a 1 M$_\odot$ − 1 M$_\odot$ stellar binary's e (top), P$_{orb}$ (middle), and P$_{rot}$ (bottom) for the CPL (blue) and CTL (orange) model. The blue (CPL) and orange (CTL) vertical dashed lines denote when the stellar binary tidally locks. Both the CPL and CTL model predict the same qualitative evolution. The rotational evolution differs, however, as under the CPL model, the binary tidally locks into a synchronous orbit as $e < \sqrt{1/19}$, e.g. Eq. (20), while the CTL model predicts supersyncronous rotation due to the CTL model's equilibrium period eccentricity dependence (see Eq. (22)).

old Orion Nebula Cluster (Stassun et al. 1999; Herbst et al. 2001, 2002; Rodríguez-Ledesma et al. 2009). We compute the secondary star's mass by uniformly sampling the mass ratio over [0.1, 1] following observations of mass ratios in low-mass binaries (Raghavan et al. 2010; Moe & Kratter 2018). Given the inherent uncertainty in and complexity of the formation of short-period binaries (e.g. Bonnell & Bate 1994; Bate 2000; Bate et al. 2002; Moe & Kratter 2018) and the potential for dynamical processing via tides or stellar close encounters (e.g. Mardling & Aarseth 2001; Hurley et al. 2002; Ivanova et al. 2005; Meibom & Mathieu 2005), we take an agnostic approach to the initial orbital configuration by uniformly randomly sampling the initial eccentricity (e) over [0.0, 0.3], consistent with eccentricities of field binaries that likely have not been tidally-processed (Raghavan et al. 2010). Although the CTL model is applicable for $e \gtrsim 0.3$, the CPL model is not and can predict qualitatively incorrect evolution in that regime (see Section 4.1 in Leconte et al. 2010), so we restrict $e \leq 0.3$ to allow us to compare both models. We uniformly sample the initial P$_{orb}$ over [3, 100] d and do not consider P$_{orb} < 3$ d as these binaries are likely to have a tertiary companion (Tokovinin et al. 2006) which can significantly impact the inner binary's dynamical evolution (e.g. Fabrycky & Tremaine 2007; Muñoz & Lai 2015; Martin et al. 2015; Hamers et al. 2016; Moe & Kratter 2018).

Values for stellar tidal Qs and τs for low-mass stars are highly uncertain due to complex viscous evolution within the stars (Ogilvie & Lin 2007), and can differ for stars of the same spectral class (Barker & Ogilvie 2009). These parameters can also vary as a function of stellar mass or age (Bolmont & Mathis 2016; Van Eylen et al. 2016), likely due to low-mass stars' evolving convective regions where the tidal dissipation predominantly occurs (Zahn 2008). Typical values of Q and τ for Sun-like stars are estimated to be of order $Q \approx 10^6$ and $\tau \approx 0.1$ s, respectively (e.g. Meibom & Mathieu 2005; Ogilvie & Lin 2007; Jackson et al. 2008), however a range of values exist in the literature. Therefore, we consider a wide range of tidal parameters by sampling stellar tidal Qs log-uniformly over [$10^4, 10^8$] and τ log-uniformly over [$10^{-2}, 10$] s. There is no general expression to compute Q as a function of τ, or vice versa, except in some special cases where approximations exist, e.g. Eqn. (2) from Heller et al. (2011). All stars have an initial age of 5 Myr unless stated otherwise as by this time, the gaseous protoplanterary circumbinary disk that can drive significant dynamical evolution in the binary (e.g. Fleming & Quinn 2017) would likely have dissipated (Haisch et al. 2001). We also perform a smaller subset of simulations to illustrate the behaviour of our coupled model and

describe their initial conditions as we introduce them. All code used to run simulations and generate figures is available online.[2]

4. RESULTS

4.1. *Interaction Between Magnetic and Tidal Braking: Subsynchronous Rotation*

Here we focus on binaries in the "weak tides" regime, i.e. long P_{orb} and large Q or small τ, to identify the boundary between evolution dominated by tides or magnetic braking via analytic calculations and simulations.

4.1.1. *Analytic Torque Balance*

In the weak tides regime, spin-down due to magnetic braking will drive the stellar P_{rot} past P_{eq}, resulting in subsynchronous rotation, $P_{rot} > P_{eq}$. For long P_{orb}, the stars will be slowly-rotating and in the unsaturated regime (Matt et al. 2015). Since magnetic braking scales as P_{rot}^{-3} for unsaturated rotators, e.g. Eqn. (2), magnetic braking torques weaken as the stellar rotation slows down, so at some P_{rot}, tidal torques will balance magnetic braking, producing a long-lasting state of subsynchronous rotation. We compute the P_{rot} at which this balance occurs as a function of P_{orb}, k_2, and τ in § A by setting the sum of Eqn. (16) and Eqn. (2) equal to 0, considering tidal torques under the CTL formalism. For simplicity, we assume both stars are solar-mass with 0 obliquity, a circular binary orbit, and that the torque balance occurs while the stars are on the main sequence where stellar properties change slowly. Although solar mass stars are the most massive stars we consider in this work, and hence will have the strongest tidal torque for a given tidal dissipation parameter and P_{orb}, they can still exhibit subsynchronous rotation and serve as a useful end member case to examine here and in simulations below. We display the results of this calculation in Fig. 3, normalizing P_{rot} by P_{eq}, which for binary stars with 0 obliquity on circular orbits is simply P_{orb}.

Our calculations show that subsynchronous rotation occurs across a wide range of tidal parameters and P_{orb}. In general as tides weaken, i.e. increasing P_{orb} and/or decreasing $\log_{10}(k_2\tau)$, tidal and magnetic braking torques balance at longer P_{rot}. For strong tides, $\log_{10}(k_2\tau) \gtrsim -1$, tidal torques overpower magnetic braking for $P_{orb} \lesssim 40$ d, tidally locking binaries into synchronous rotation. For our fiducial values of $k_2 = 0.5$ and $\tau = 0.1$ s (white dashed line in Fig. 3), solar-twin binaries will rotate subsynchronously for $P_{orb} \gtrsim 20$ d, with more severe subsynchronism at longer P_{orb}. This simple
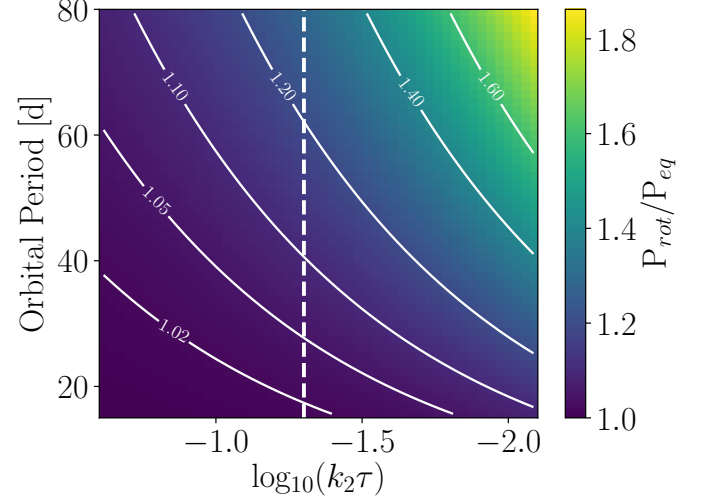
Figure 3. The stellar P_{rot}, normalized by P_{eq}, at which the torques due to magnetic braking and tides balance for a 1 $M_\odot - 1$ $M_\odot$ binary on a circular orbit according to Eqn. A4. The white dashed line indicates our fiducial values for k_2 and τ, 0.5 and 0.1 s, respectively, that we adopt in the simulations in § 4.1.2.

calculation, however, does not account for stellar evolution or secular tidal orbital evolution, e.g. tidal friction that will shrink the orbit, gradually strengthening tidal torques, so we turn to simulations to characterize this evolution.

4.1.2. *Torque Balance*

We simulate the full coupled stellar-tidal evolution of 1 $M_\odot - 1$ $M_\odot$ binaries on initially circular orbits to examine how stellar binaries evolve towards subsynchronous rotation. In Fig. 4, we plot P_{rot}, normalized by P_{eq}, and its time derivative for $P_{orb} \in [5, 60]$ d modeled using both the CPL (solid line, $Q = 10^6$) and CTL (dashed line, $\tau = 0.1$ s) models. Both tidal models predict that binaries with $P_{orb} < 10$ d will tidally lock within 100 Myr, in agreement with observations (Meibom & Mathieu 2005) and previous theoretical work (Zahn & Bouchet 1989). The CPL model predicts that all binaries tidally lock, even out to $P_{orb} = 60$ d, indicating that tidal locking is not necessarily restricted to short P_{orb} systems. As anticipated by our analytic calculations, the CTL model predicts subsynchronous rotation for $P_{orb} \geq 20$ d as magnetic braking overpowers tidal torques. For $P_{orb} = 20$ d, magnetic braking pushes $P_{rot}/P_{eq} \approx 1.05$, with the maximum value set by the torque balance. As shown in § 4.1.1, the peak P_{rot}/P_{eq} grows for longer P_{orb} since tides weaken with increasing binary separation, e.g. Eqn. (18), allowing magnetic braking to dominate the spin evolution.
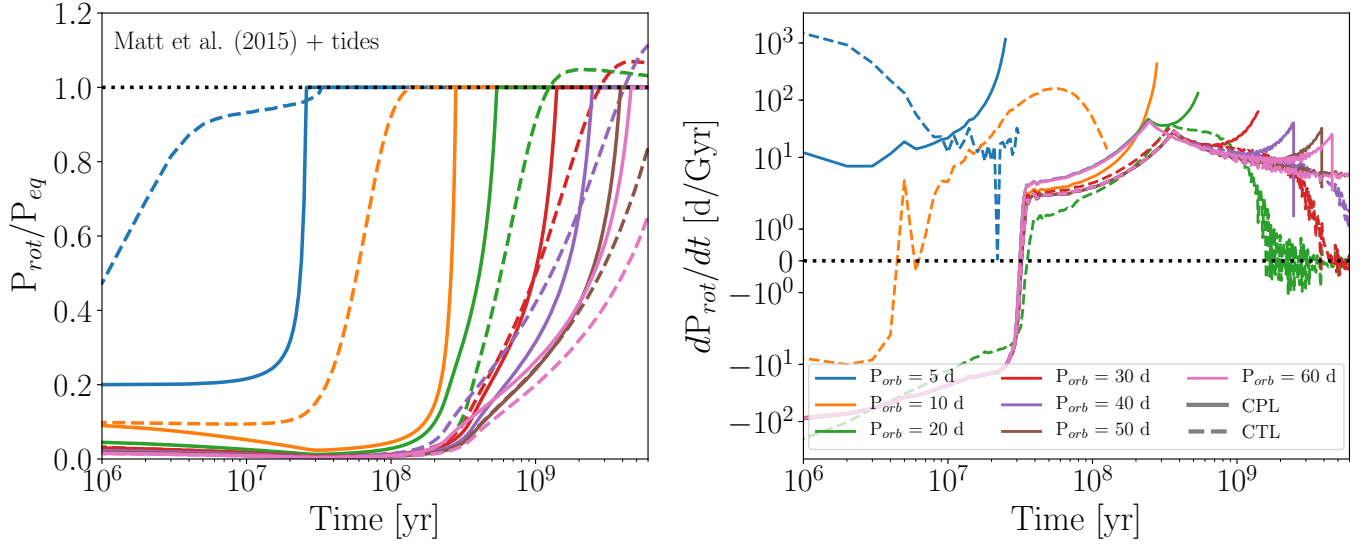
Figure 4. Evolution of stellar P_{rot}, normalized by P_{eq} (see Eqn. (20) and Eqn. (22)), for initial circular binary orbits according to the CPL (solid) and CTL (dashed) models with $Q = 10^6$ and $\tau = 0.1$ s, respectively, using the Matt et al. (2015) magnetic braking model. Left: P_{rot}/P_{eq} for stars with P_{orb} ranging from 5 d to 60 d. The black dotted line indicates the tidally locked state. Right: Net P_{rot} derivative due to stellar evolution, tidal torques, and magnetic braking. We truncate each curve when the binary tidally locks. The legend denotes the initial binary orbital period and we note that the orbital periods do not vary by more than a few percent over the course of the simulations.

For $P_{orb} \leq 10$ d, both the CPL and CTL models predict that the binaries lock into synchronous rotation. For all P_{orb}, the CPL models tidally lock whereas the CTL model predicts subsynchronous rotation that persists for Gyrs.

Subsynchronous rotation does not persist indefinitely, however, as P_{rot} eventually decreases back towards the tidally locked state in the long-term due to a combination of three simultaneous physical effects. First, magnetic braking weakens at long P_{rot} as its torque scales as P_{rot}^{-3} for unsaturated rotators (Matt et al. 2015). Second, as P_{rot} increases further from the tidally locked state, tidal torques strengthen as they try to force P_{rot} back towards P_{eq} (see Eqn. (16)). Third, when $P_{rot} > P_{eq}$, tides transfer angular momentum from the orbit into stellar rotations, decreasing P_{orb}, gradually strengthening tidal torques that strongly depend on the binary separation as $a^{-6.5}$. These effects combine to shift the balance of power from magnetic braking-controlled stellar spin down to tidal torques spinning-up stars, shepherding them towards P_{eq} in the long-term.

We can see this process unfold in the right panel of Fig. 4 where we plot the total P_{rot} time derivative due to tidal torques, stellar evolution, and magnetic braking. Early on, $\dot{P}_{rot} < 0$ as stars contract along the pre-main sequence until about 60 Myr when the stars reach the zero age main sequence. Tides and magnetic braking then combine to spin down stars towards the tidally locked state. For the CTL models with $P_{orb} > 10$ d, $\dot{P}_{rot} > 0$ as magnetic braking dominates, driving the stars into subsynchronous rotation. In the long-term, $\ddot{P}_{rot} < 0$, however, as the three processes de-

scribed above gradually strengthen tidal torques relative to magnetic braking. Tidal torques eventually overpower magnetic braking, seen as a slight negative P_{rot} derivative, slowly driving P_{rot} back towards P_{eq}, producing a population of subsynchronous rotators that can persist for Gyrs. We explore this point further in § 4.2.1.

4.2. Influence of P_{orb}, Q and τ

We next examine how P_{rot} evolution in stellar binaries depends on P_{orb} and the strength of tidal dissipation, parameterized by Q and τ for the CPL and CTL models, respectively. In Fig. 5, we bin our simulation results after the full 7 Gyr evolution by P_{orb} and Q or τ and compute the median P_{orb}/P_{rot} in each bin, marginalizing over all other parameters.

Spin-orbit synchronization is the typical outcome for binaries with $P_{orb} < 10$ d according to the CPL model for most values of Q. The strong tidal torques predicted by the CPL model can even tidally lock binaries out to $P_{orb} \gtrsim 80$ d for $Q < 10^5$, well beyond the expected limit of 20 d (Meibom et al. 2006). According to the CTL model, binaries with $P_{orb} < 10$ d typically tidally lock for $\tau \gtrsim 0.1$ s, and seldomly tidally lock for $P_{orb} > 20$ d, except for systems with strong tides, $\tau \gtrsim 3$ s. Both models predict a substantial population of subsynchronous rotators (red regions in Fig. 5, $P_{rot} > P_{orb}$), consistent with magnetic braking dominating weak tidal torques. The population of supersynchronous rotators (blue re-

gions in Fig. 5, $P_{rot} < P_{orb}$) with $P_{orb} > 60$ d does not in general correspond to binaries tidally locking into supersynchronous rotation, but rather, typically arises from the combination of weak tidal torques and magnetic braking not spinning down stars enough for P_{rot} to be close to the tidally locked state. At a given age, longer P_{orb} binaries will tend to rotate faster as they experience weaker tidal torques, and hence require longer to spin down towards the tidally locked state.

Both tidal models predict a population of nearly synchronous rotators near $P_{orb} \approx 60$ d. This population corresponds to the evolution described in § 4.1 in which magnetic braking initially spins down stars past the tidally locked state, but in the long-term, tidal torques spin up the stars, shepherding them towards the tidally locked state. This process can keep stellar $P_{rot} \gtrsim P_{eq}$ for several Gyrs or longer, depending on the P_{orb} and Q or τ (see Fig. 4, § 4.2.1).

We isolate the impact of Q and τ on the spin-orbital state of tidally interacting stellar binaries by binning our CPL and CTL simulation results after 7 Gyr of evolution by P_{orb} and P_{orb}/P_{rot} in Figures 6 and 7, respectively. In these figures, we estimate the typical strength of tidal torques, using Q and τ as a proxy, that can produce various spin-orbital states. For the CPL simulations depicted in Fig. 6, synchronous and supersynchronous rotators have systematically low Qs, typically $Q < 10^6$, as strong tidal torques are required to tidally lock these binaries. For $P_{orb} < 10$ d, there are no rotators with $1.0 < P_{orb}/P_{rot} < 1.5$, nor do any stars have $P_{orb}/P_{rot} > 1.5$ for $P_{orb} < 60$ d, as in the CPL model, binaries with eccentric orbits can only tidally lock into a 1:1 or 3:2 spin-orbit commensurability, see Eqn. (20).

Subsynchronous rotators have systematically larger Qs, typically $Q > 10^6$, and hence experience weak tidal torques that are dominated by magnetic braking. Subsynchronous rotation can occur under the CPL model for binaries with $P_{orb} < 50$ d. In this regime, the median Q tends to increase with decreasing P_{orb}/P_{rot}, except near the tidally locked state, as magnetic braking dominates weaker tidal torques, yielding longer P_{rot}. This trend reverses at longer $P_{orb} > 60$ d where supersynchronous rotation arises from the inability of tidal torques and magnetic braking to spin-down stars enough to approach the tidally locked state by the end of the simulation. In this case, the more supersynchronous the rotation, the weaker the tidal torques must be, and hence the larger the Q must be.

According to the CTL model simulations, depicted in Fig. 7, many binaries tidally lock for $P_{orb} \lesssim 20$ d when $\tau \gtrsim 0.1$ s, with some tidally locking up to $P_{orb} \approx 50$ d when $\tau \gtrsim 1$ s. Subsynchronous rotation typically occurs

for stars with $\tau < 0.1$ s. Similar to the behavior depicted in Fig. 6, longer P_{rot} are produced by binaries with weaker tidal interactions since P_{orb}/P_{rot} decreases monotonically with τ for $P_{orb} < 40$ d. For $P_{orb} > 50$ d, magnetic braking dominates the evolution seen in the diagonal sequence with a median $\tau \approx 0.1$ s, a value that is typically insufficient for tides to strongly influence the evolution given the wide orbital separations. The shape of this diagonal region arises from the combination of magnetic braking and our flat initial P_{orb} distribution. In this P_{orb} regime, most binaries rotate supersynchronously as tides and magnetic braking fail to sufficiently spin down the stars by the age of the system. At longer P_{orb}, some binaries can strongly tidally-interact, but these systems require extreme tidal $\tau \gtrsim 10$ s. Unlike the CPL simulations depicted in Fig. 6, these binaries with $P_{orb} \approx 90$ d are not tidally locked as the tides are still not strong enough to lock the system. We explore this point further in § 4.3. We do not often observe $P_{orb}/P_{rot} \gtrsim 1.5$ as we only consider eccentricities up to $e = 0.3$, limiting how rapid supersynchronous systems can rotate according to Eqn. (22).

4.2.1. Subsynchronous Rotation at Short P_{orb}

As seen in Fig. 5, subsynchronous rotation can even occur for short P_{orb} binaries, where tidal-locking is the expectation, if the tidal torques are sufficiently weak. In Fig. 8, we examine subsynchronous rotation in short P_{orb} binaries by displaying the P_{rot} evolution for a $P_{orb} = 7.5$ d binary for various tidal dissipation parameters. Subsynchronous rotation occurs in general for weak tidal torques, $Q > 10^7$ or $\tau < 0.1$ s in these cases, and is not restricted to long P_{orb} binaries. Previous theoretical studies have also predicted subsynchronous rotation in short P_{orb} binaries arising from the balance between tidal torques and magnetic braking (e.g. Habets & Zwaan 1989; Zahn 1994; Keppens 1997) suggesting that this behavior is not an artifact of our choice of tidal or magnetic braking models, but rather a general outcome of the competition between magnetic braking and tidal evolution in low-mass binaries. Short P_{orb} subsynchronous rotators can eventually tidally lock after several Gyrs, e.g. the $Q = 10^8$ case in Fig. 8, via the mechanism described above where tidal torques gradually strengthen relative to magnetic braking.

Short P_{orb} subsynchronous binaries exist in nature, such as many *Kepler* EBs (Lurie et al. (2017), see § 4.5 for further discussion), Kepler-47 (Orosz et al. 2012), EPIC 219394517 (Torres et al. 2018), and in "Binary 6211" observed by Meibom et al. (2006), suggesting that this theoretical observation is real and borne out in nature. Spin-orbit synchronization should therefore not
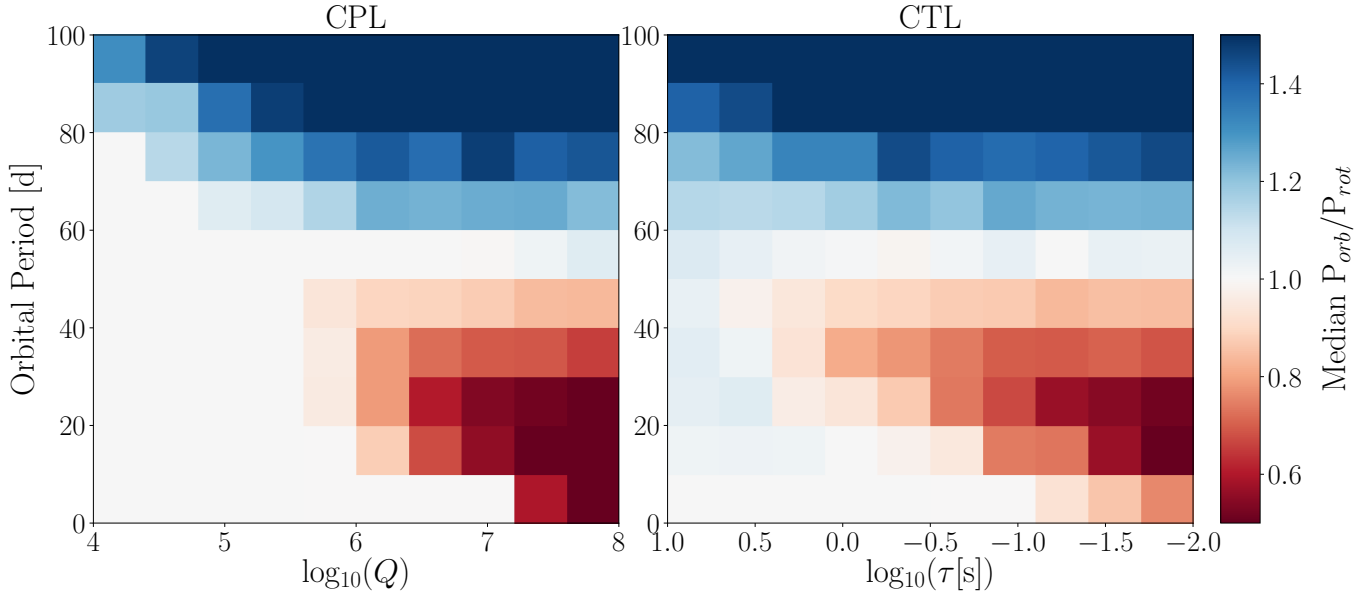
Figure 5. Median P_{orb}/P_{rot} at the end of the simulation according to the CPL (left) and CTL (right) models binned by $\log_{10}(Q)$ and $\log_{10}(\tau)$, respectively, and P_{orb}. For $P_{orb} < 10$ d, the CPL model predicts that most systems will tidally lock into synchronous rotation, whereas the CTL model requires $\tau \geq 0.1$ s to tidally lock. For large Q ($> 10^7$) and small τ ($\tau < 0.1$ s), weak tidal torques cannot prevent magnetic braking from spinning down stars past the tidally locked state, producing a population of subsynchronous rotators (red regions, $P_{rot} > P_{orb}$).

be assumed for short P_{orb} binaries and sunsynchronous rotation should be expected in many tidally interacting binaries. We explore these effect further and compare our theory to observations of *Kepler* EBs in § 4.5.

4.3. P_{rot} Distribution of a Synthetic Population of Stellar Binaries

Here we examine how the competition between tidal torques and magnetic braking shape the P_{rot} distribution of low-mass stellar binaries. We consider two cases where tidal torques dominate: "Locked", where $P_{rot} = P_{eq}$, and "Interacting", where P_{rot} is within 10% of P_{eq} as in this regime, tides are likely shepherding P_{rot} towards the tidally locked state as we demonstrated in § 4.1. We refer to the remaining binaries as "not locked" as magnetic braking and stellar evolution likely dominate their angular momentum evolution. In Fig. 9 and Fig. 10, we plot P_{rot} as a function of mass for the primary stars in stellar binaries for both the CPL and CTL model, respectively, integrated to system ages uniformly sampled over $1 - 7$ Gyr, consistent with ages of stars in the *Kepler* field (Chaplin et al. 2014).

Both models predict a substantial population of tidally locked fast rotators with $P_{rot} \lesssim 20$ d, with tidally locked stars systematically rotating faster (median CPL, CTL $P_{rot} = 22.6$ d and 8.8 d) than not locked (median CPL, CTL both $P_{rot} = 32.4$ d) binaries. The CTL model predicts that the majority of tidally locked binaries, 83%, lock into rapid rotation with $P_{rot} \lesssim 20$ d,

typically in short P_{orb} binaries where tidal torques are strongest. The CPL model, however predicts that binaries can tidally lock into a wide range of rotation states as only 46% of locked binaries have $P_{rot} < 20$ d, while the rest can lock out to $P_{rot} \approx 100$ d in long P_{orb} binaries. More massive stars are more likely to tidally lock compared to less massive stars as tidal torques scale with the stellar masses and as R^5, with R increasing with stellar mass. This feature is seen in the enhanced density of locked systems at larger masses for both tidal models, but in particular for the CPL model. We highlight this enhanced density of locked binaries in systems with more massive primaries in the marginalized mass distributions in the top panels of Fig. 9 and Fig. 10.

The interacting population tends to rotate more slowly than the not locked population as at short P_{orb}, and hence P_{rot}, binaries preferentially tidally lock due to stronger tidal torques. At longer P_{orb}, weaker tidal torques allow magnetic braking to spin down the stars past P_{eq}, with tidal torques eventually strengthening enough to shepherd P_{rot} towards P_{eq} via the mechanism discussed in § 4.1. The CPL and CTL models predict that 31% and 24% of stars, respectively, are either tidally locked or interacting, demonstrating that tidal torques play a pivotal role in shaping the angular momentum evolution in stellar binaries across a wide range of parameters. The P_{rot} - mass distribution for not locked binaries resembles the single star sequence
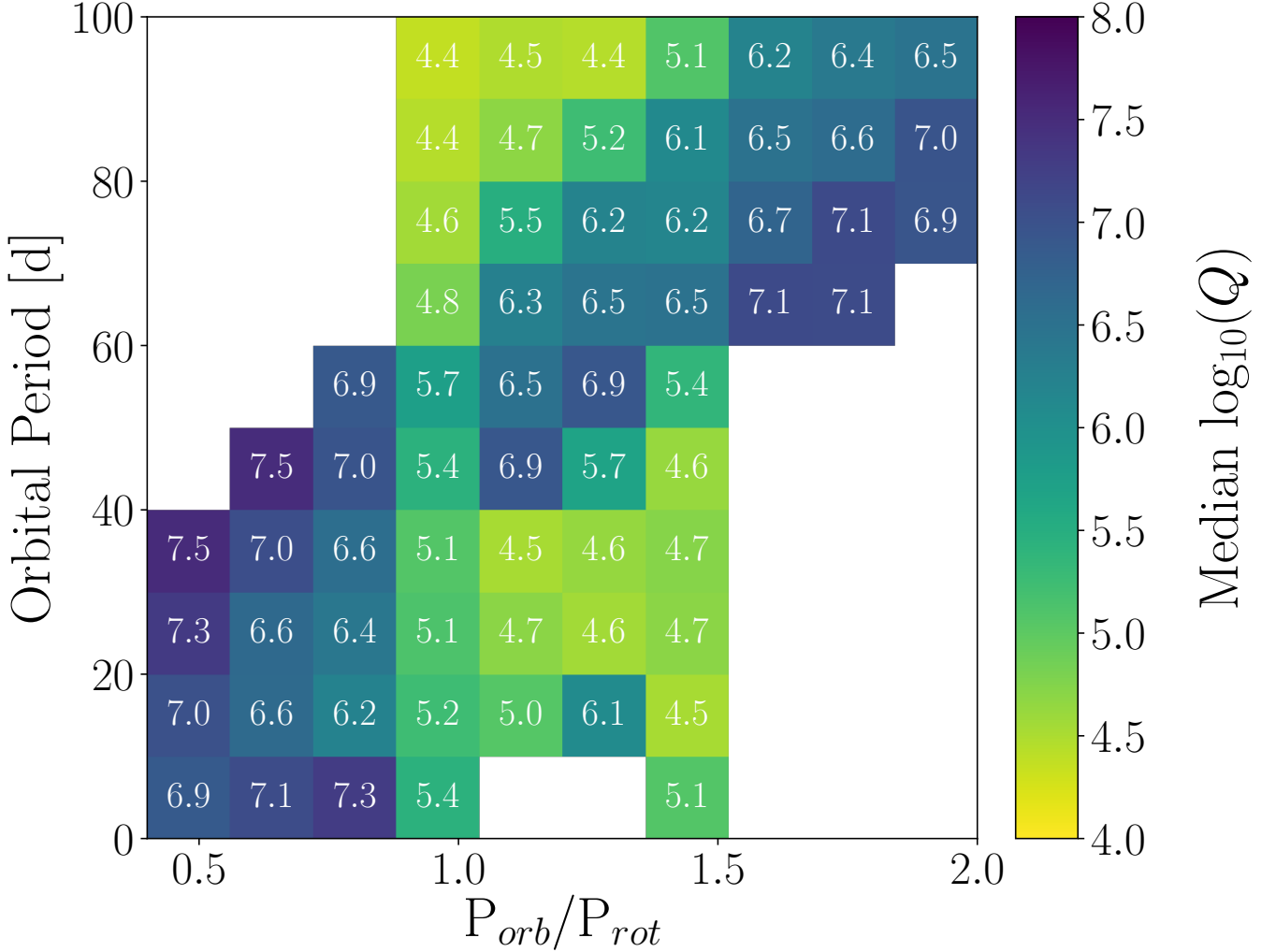
Figure 6. Median $\log_{10}(Q)$ of primary stars binned by P_{orb} and P_{orb}/P_{rot} evolved using the CPL model.

as magnetic braking and stellar evolution dictate their angular momentum evolution.

Tidal locking is not limited to $P_{orb} \lesssim 20$ d, however, as we find stellar binaries can tidally lock over a wide range of P_{rot} up to $P_{rot} = P_{orb} \approx 100$ d according to the CPL model, producing a slow-rotating population above the P_{rot} distribution envelop of solar-mass single stars. This behavior is consistent with observations of P_{rot} in *Kepler* eclipsing binaries by Lurie et al. (2017) who find tentative evidence that binaries can tidally lock up to their detection limit of $P_{orb} = P_{rot} = 45$ d. Under the CTL model, however, binaries predominantly tidally lock out to only $P_{orb} \approx 20$ d, although binaries with more massive primaries can occasionally lock, or at least tidally-interact, out to $P_{orb} \approx 80$ d. We highlight this behavior with a histogram of locked and interacting binaries over P_{rot} for both tidal models in Fig. 11. The CTL model predicts fewer tidally locked binaries at longer P_{rot}, concentrating most of the locked CTL dis-

tribution's density at short P_{rot}, whereas the CPL distribution has a heavy tail extending towards longer P_{rot}. The CPL model, however, predicts larger tidal-locking rates than the CTL model as seen in the enhanced numbers of tidally locked binaries at low P_{rot} Fig. 9 compared with Fig. 10. The presence of $P_{orb} > 20$ d locked population, or lack there of, could be a powerful observational discriminant between which equilibrium tidal model acts in low-mass stellar binaries. We discuss this point further in § 4.6.

4.4. Deviations From Single Star P_{rot} Evolution: Implications for Gyrochronology

We compare the P_{rot} and age distributions of tidally interacting stellar binaries from our CPL and CTL simulations with that of single stars to gauge the impact of tidal torques on driving P_{rot} distributions away from that of single stars and what implications that may have for estimating stellar ages using gyrochronology. We
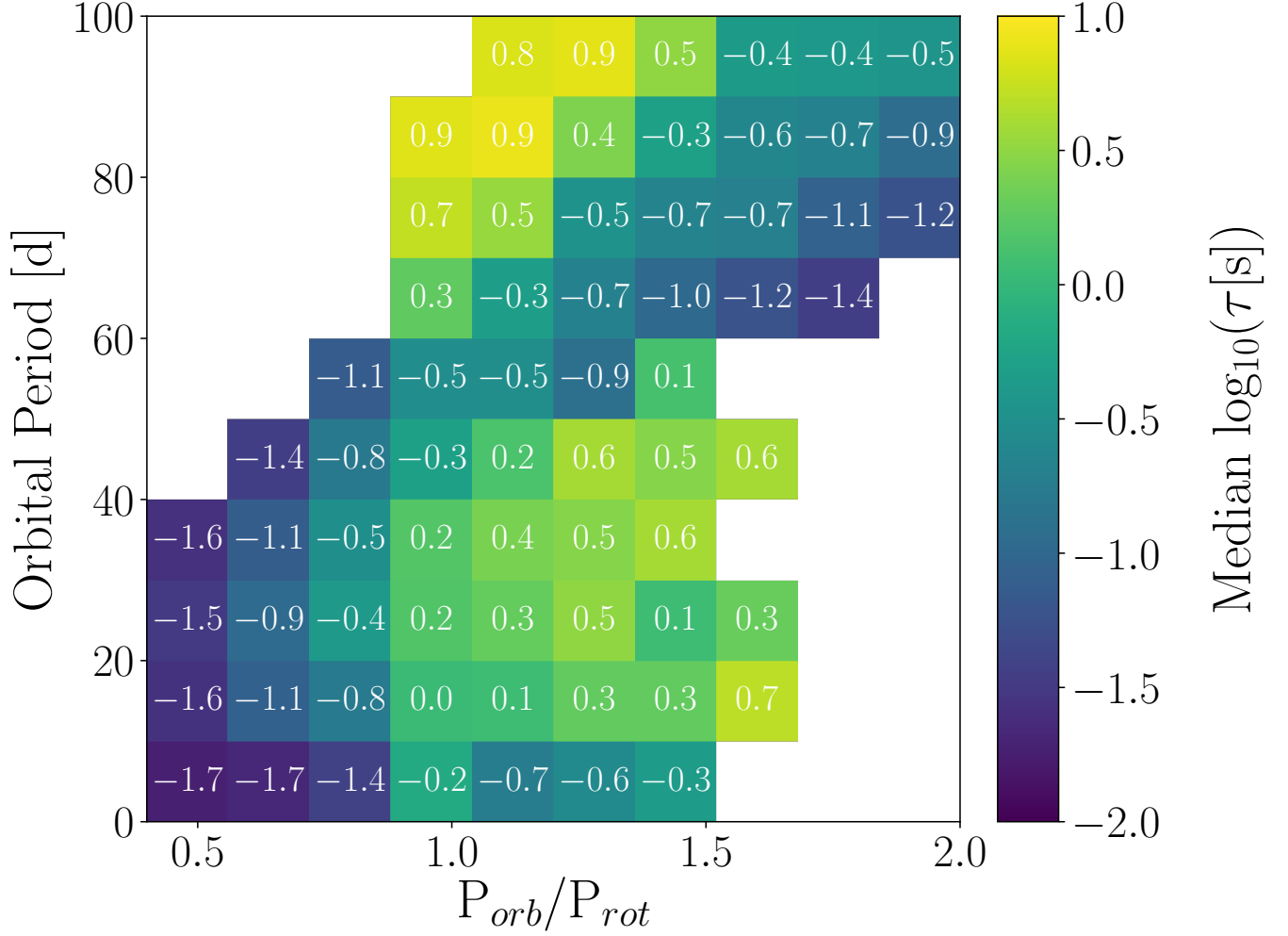
Figure 7. Same format as Fig. 6, but for $\log_{10}(\tau[s])$ under the CTL model.

simulate 10,000 single star systems according to the evolution described in § 2.1 with initial conditions sampled from the same mass and P_{rot} distributions used for the binary simulations described § 2. In Fig. 12, we display P_{rot} as a function of mass and age for binaries simulated using both the CPL and CTL model and for single stars.

In binaries, tidal torques tend to drive the P_{rot} evolution away from that of single stars and towards P_{eq}, either maintaining rapid rotation in tidally locked short P_{orb} systems, or working with magnetic braking to slow P_{rot} beyond that of single stars of the same age. The impact of tidal torques on the binary P_{rot} distribution is clear: strong tidal torques in short P_{orb} binaries produce a substantial population of rapid rotators with $P_{rot} \lesssim 20$ d. Except for stars with ages $\lesssim 1$ Gyr, or young late M-dwarfs who are either contracting along the pre-main sequence or have just reached the main sequence, our single star simulations fail to produce a population of rapid rotators. This theoretical result is consistent with

Simonian et al. (2018) who find that the population of *Kepler* stars with $P_{rot} < 7.5$ d is likely dominated by tidally interacting binaries. The influence of tides extends to longer P_{orb} systems producing a slowly-rotating population above the upper envelope of the single star sequence for M $\gtrsim 0.6$ $M_{\odot}$, e.g. Fig. 9 and Fig. 10, and is a population that single-star models fail to produce.

In the single star population, there is a clear monotonic relation between P_{rot} and age, with older stars rotating more slowly, a trend that is borne out in nature and is the critical assumption of gyrochronology methods that link P_{rot} to stellar ages via the magnetic braking-driven long-term spin down of low-mass stars (e.g. Skumanich 1972; Barnes 2003, 2007; Mamajek & Hillenbrand 2008; Barnes 2010; Meibom et al. 2015). This trend is a generic outcome of magnetic braking and is not specific to our choice of magnetic braking model. In stark contrast, both tidal models predict that age does not always strongly correlate with P_{rot} as tidally
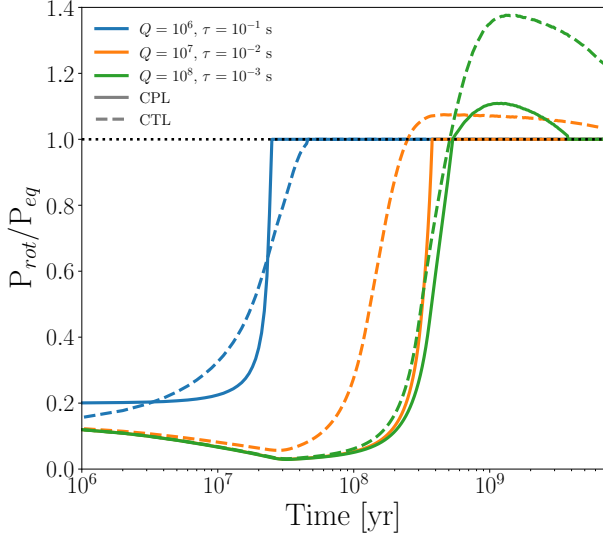
Figure 8. Evolution of stellar P_{rot}, normalized by P_{eq} (see Eqn. (20) and Eqn. (22)), for initial circular binary orbits with initial $P_{orb} = 7.5$ d according to the CPL (solid) and CTL (dashed) models for several values of Q and τ, respectively, using the Matt et al. (2015) magnetic braking model. Systems with strong tidal torques tidally lock, whereas in systems with weaker tidal torques (larger Q and smaller τ, respectively), magnetic braking initially overpowers tidal torques, spinning down the stars past the tidally locked state, resulting in subsynchronous rotation.

interacting binaries, at a given primary star mass and P_{rot}, can assume a wide range of ages, especially for $P_{rot} \lesssim 20$ d.

We quantify the impact of binarity on gyrochronology age estimates in Fig. 13 by computing the percent difference between the mean ages of single and binary stars, for both tidal models, in mass and P_{rot} bins for the populations depicted in Fig. 12. This quantity, referred to here as the "Relative Age Error", represents the systematic error incurred by assigning a tidally interacting binary star the age expected for single stars at a given mass and P_{rot}. For this comparison, we select the subset of tidally locked and tidally interacting binaries as classified in Fig. 9 and Fig. 10.

For most values of P_{rot}, gyrochronology methods systematically underestimate the ages of tidally interacting binaries, with the relative age error increasing with decreasing P_{rot} and increasing with primary star mass. For binaries with $P_{rot} \lesssim 30$ d, gyrochronology ages are underestimated by 50%, with this error growing to 300% for $P_{rot} \approx 10$ d. For slow rotators with $P_{rot} \gtrsim 40$ d, gyrochronology ages are slightly overestimated by up to 25%, with the largest errors occurring for near solar-mass primary stars where tides and magnetic braking combine to spin down binary stars. The relative age
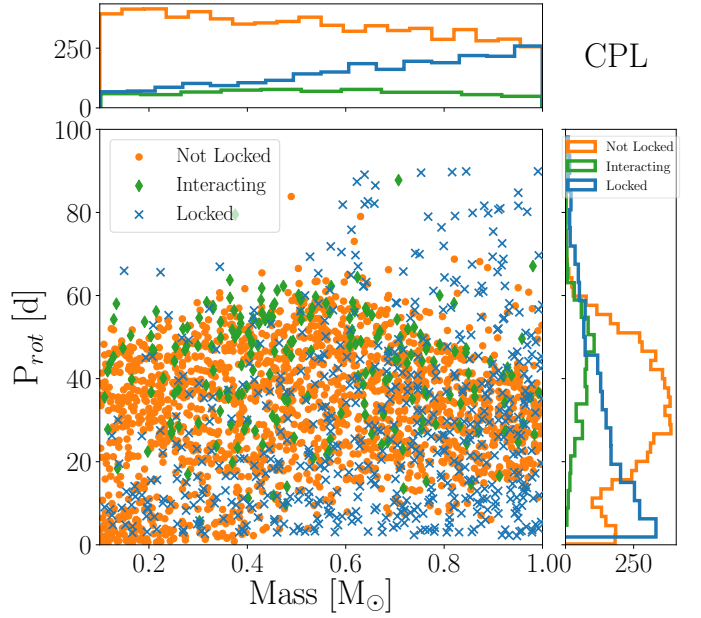

Figure 9. Rotation state for tidally locked (blue, $P_{rot} = P_{eq}$), interacting (green, P_{rot} within 10% of P_{eq} and not locked), and not locked (orange, remainder of binaries) stellar binaries. Left: P_{rot} as a function of stellar mass and age according to our CPL simulations integrated to system ages uniformly sampled over $1 - 7$ Gyr. Right: Marginalized P_{rot} distribution for each case. Top: Marginalized mass distributions.
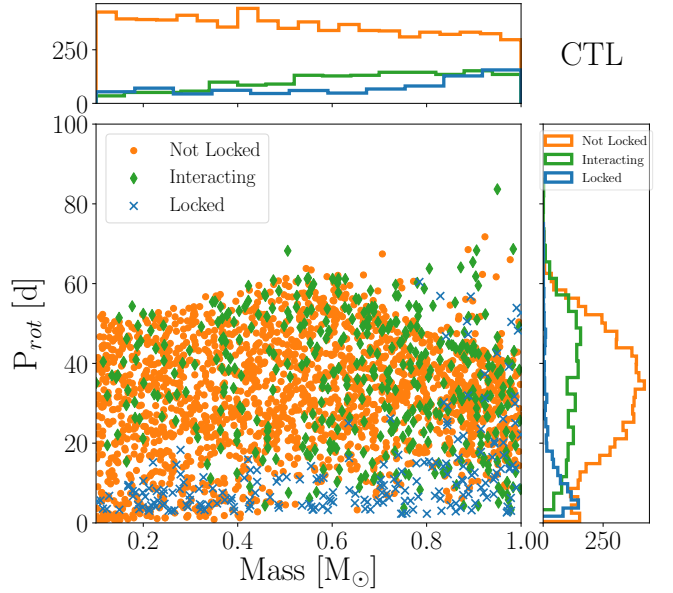

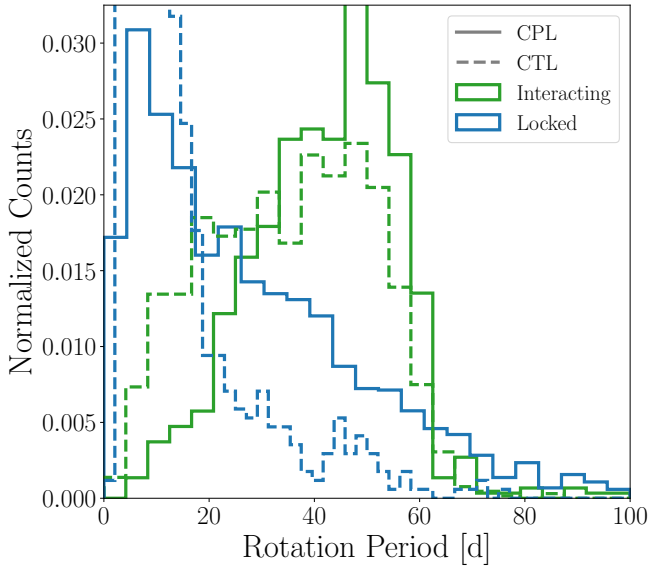**Figure 10.** Same format as Fig. 9, but for the CTL simulations.

Figure 11. P_{rot} distribution for tidally locked (blue) and interacting (green, P_{rot} within 10% of P_{eq} and not locked) binaries according to the CPL (solid line) and CTL (dashed line) models.

errors would be more pronounced for the most rapidly-rotating stars, e.g. tidally interacting near-solar mass binaries with $P_{rot} \lesssim 10$ d, however, our single star-only models fail to produce such rotation states.

The age distribution of binaries with $P_{rot} < 20$ d is inconsistent with that of single stars. In this range, the median ages and 68% interval are $2.3^{+2.9}_{-0.9}$ Gyr and $2.4^{+3.0}_{-1.1}$ Gyr according to the CPL and CTL models, respectively, compared to the much younger single stars with ages of $1.6^{+0.8}_{-0.4}$ Gyr. We highlight this dichotomy in Fig. 14 by plotting a histogram of system ages from Fig. 12 for single or primary stars in binaries with $P_{rot} < 20$ d.

Tidal torques pose a fundamental problem for inferring ages of stars via gyrochronology. Regardless of the choice of equilibrium tidal model or magnetic braking model, stellar binaries readily tidally lock, or at least strongly tidally-interact, across a wide range of P_{orb} and primary star masses, decoupling P_{rot} from age. For example, if one observed a rapidly rotating star with $P_{rot} \lesssim 20$ d, gyrochronology models would predict ages $\lesssim 1.6$ Gyr. If the star is actually an unresolved binary, as could be the case for many *Kepler* rapid rotators (Simonian et al. 2018), it would likely be tidally locked, decoupling P_{rot} from age, causing the predictions of gyrochronology models to fail. This effect is most likely to manifest in rapid rotators ($P_{rot} < 20$ d), but persists across all P_{rot} up to 100 d, producing a contaminating signal, e.g. Fig. 12 and Fig. 13.

In general, it is difficult to accurately determine if a source is single star or a stellar binary via longterm photometric monitoring, e.g. via *Kepler* or *TESS*, as only a small fraction of stars in binaries will occult one another. Observations of the binarity of field stars by Raghavan et al. (2010) and Duchêne & Kraus (2013) indicate that roughly half of stars are in stellar binaries, with 10% of these binaries having $P_{orb} \lesssim 100$ d, suggesting that unless one accounts for binarity, stellar binaries will produce a contaminating signal in any study of stellar rotation periods and any ages inferred via gyrochronology are potentially subject to systematic errors. Moreover, this problem could be more significant as Simonian et al. (2018) found that most rapid rotators with $P_{rot} \leq 7.5$ d in the *Kepler* field are consistent with tidally-synchronized photometric binaries, suggesting that binary contamination in P_{rot} studies could be widespread. We caution that any application of gyrochronology methods to predict ages for stars, especially those with $P_{rot} \lesssim 20$ d, should rule out or account for stellar binarity, or otherwise risk deriving systematically incorrect ages. Tidal torques do not just produce spin-orbit synchronization at short P_{orb}, but can produce a rich variety of rotation states that deviate from the expected long-term spin-down experienced by single stars, e.g. Fig. 6 and Fig. 7. We recommend that the application, or calibration, magnetic braking models to a sample of stellar rotation periods control for binarity.

4.5. *Comparison to Kepler*

We compare our simulation results to P_{rot} measurements of primary stars in *Kepler* low-mass eclipsing binaries by Lurie et al. (2017) to gauge if our model predictions, which by design populate a wide, but physically-plausible, region of parameter space, can reproduce features observed in the data. Lurie et al. (2017) measured 816 rotation periods for primary stars in *Kepler* EBs with star spot modulations and visually inspected each light curve to ensure their accuracy. The Lurie et al. (2017) dataset is the largest homogenous set of P_{rot} measurements available for low-mass stellar binaries and represents the state of the art benchmark for studies of the influence of tides on P_{rot} in stellar binaries. We compare our results to the $P_{1,min}$ P_{rot} values reported by Lurie et al. (2017) as the authors demonstrated that these values are likely to be close to the equatorial P_{rot} that we track in our simulations. In Fig. 15, we display P_{orb}/P_{rot} as a function of P_{orb} for both the CPL and CTL models where each simulation was integrated to an age uniformly sampled over $1 - 7$ Gyr, consistent with ages of *Kepler* field stars (Chaplin et al. 2014).
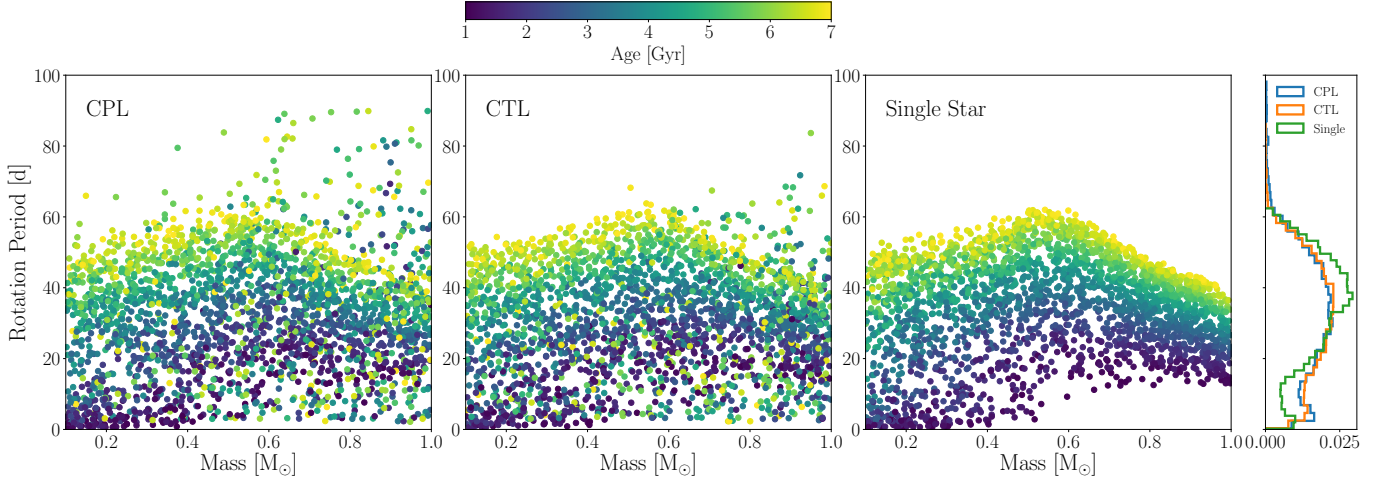
Figure 12. P_{rot} as a function of stellar mass and age according to our CPL (left), CTL (left center), and single star (right center) simulations integrated to system ages uniformly sampled over $1-7$ Gyr using the Matt et al. (2015) magnetic braking model. For each case, we only plot 2,500 systems for clarity but account for all systems when computing the marginalized distributions. Right: The P_{rot} distribution for each case, marginalized over stellar mass.
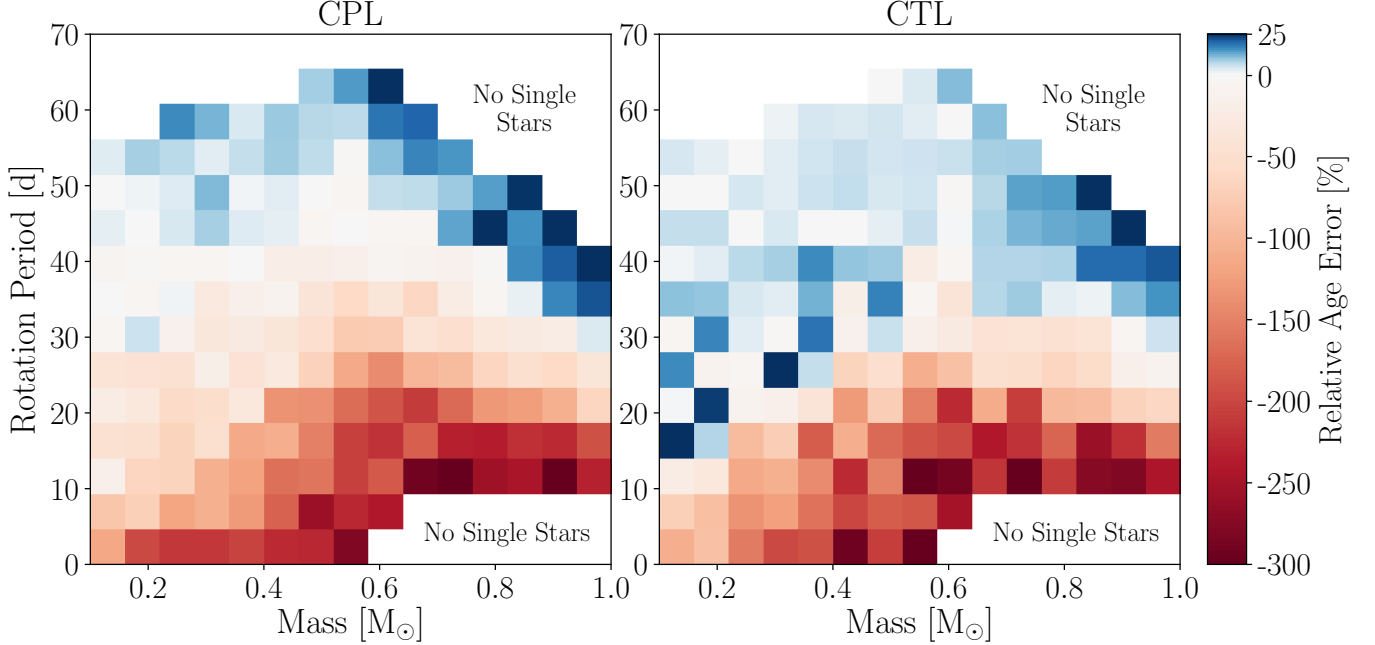

Figure 13. Relative age error between single and binary stars for both the CPL (left) and CTL (right) tidal models. The error is computed as the percent difference between the mean ages of single and tidally interacting binary stars in mass and P_{rot} bins.

Qualitatively, the CTL model appears to do a better job of reproducing features seen in the Lurie et al. (2017) data than the CPL model. The CPL model, for example, cannot produce the observed cluster of supersynchronous rotators with $P_{orb}/P_{rot} \lesssim 1.2$ for $P_{orb} < 10$ d whereas the CTL model can. Instead, owing to the its discrete P_{eq}, the CPL model predicts that all tidally locked supersynchronous rotators lie on the line $P_{orb}/P_{rot} = 1.5$. This prediction is inconsistent with

the data as no obvious spin-orbit commensurablity, aside from 1:1 synchronization, is present in the Lurie et al. (2017) data, likely because stellar convective envelopes lack a fixed shape, making resonant coupling difficult unless it occurs with internal gravity or pressure modes (Burkart et al. 2014; Lurie et al. 2017). Neither model reproduces the very supersynchronous, $P_{orb}/P_{rot} > 1.6$, binaries in the Lurie et al. (2017) data as they typically have orbital eccentricities in excess of 0.3 and are out-
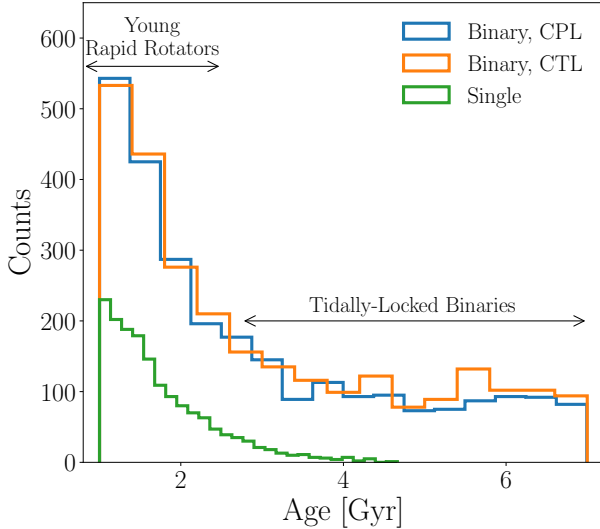
Figure 14. Histogram of rapidly-rotating ($P_{rot} < 20$ d) star ages for single and primary stars in binaries from Fig. 12. Rapidly-rotating single stars must be young (ages $\lesssim 2$ Gyr), while tidally locked rapidly-rotating binaries exhibit a wide range of ages.

side of the region of parameter space we consider. The CTL model, however, could in principle reproduce these points if they are tidally locked binaries as its P_{eq} is a continuous function of e and is applicable for large e, in contrast to the discrete P_{eq} predicted by the CPL model that is valid for smaller e. Both tidal models predict that nearly all binaries with $P_{orb} < 4$ d have circularized orbits and synchronized spins due to strong tidal torques at short stellar separations, in agreement with the Lurie et al. (2017) observations. At very short P_{orb}, in the absence of a perturbing tertiary companion, circularization and synchronization is the inevitable end state for low-mass binaries (Counselman 1973).

For $P_{orb} \gtrsim 4$ d, our models produce a substantial number of subsynchronous rotators. Although Lurie et al. (2017) argues that differential rotation creates the subsynchronous population, we find that the competition between weak tidal torques and magnetic braking described in § 4.1 naturally produces this population. The CPL model, however, struggles to populate the prominent cluster of subsynchronous rotators at $P_{orb}/P_{rot} \approx 0.9$ for $P_{orb} < 10$ d observed by Lurie et al. (2017). Lurie et al. (2017) find that 15% of their sample with $2 < P_{orb} < 10$ days has $P_{orb}/P_{rot} \in [0.84, 0.92]$, compared with 8% of our CTL population and only 2% of the CPL population.

Both models predict a large number of extremely subsynchronous rotators with $P_{orb}/P_{rot} < 0.7$ across all P_{orb} that is not present in the Lurie et al. (2017) data. Magnetic braking creates the lower limit of this subsyn-

chronous population, a line of nearly constant $P_{rot} \approx 60$ d set by how much a star can spin down over 7 Gyr, the longest age considered in our simulations. Our choice of prior distributions for both Q and τ permit very weak tidal interactions that likely gives rise to this population and suggests that our prior does not reflect the underlying distribution of stellar tidal parameters in nature. Alternatively, the data could be incomplete where our models predict slowly-rotating subsynchronous rotators as the photometric amplitude of star spot modulations tends to decrease with increasing P_{rot}, making reliable rotation periods difficult to detect (McQuillan et al. 2014; Lurie et al. 2017; Reinhold et al. 2018).

Although the CTL model seems to better reproduce the Lurie et al. (2017) data, both tidal models can reproduce features observed in the *Kepler* EB distribution, e.g. the synchronized population and subsynchronous rotators, suggesting that our models reasonably approximate the dynamical interactions of tidally-evolving, low-mass stellar binaries. Our comparison between theory and observations is limited, however, because the Lurie et al. (2017) P_{rot} data lack uncertainties and Lurie et al. (2017) approximated the EB orbital e via transit durations and ingress/egress times, potentially leading to inaccurate e determinations. Unconstrained biases in the data, e.g. the lack of long P_{orb} binaries, further inhibit our ability to compare our predictions with the data. Moreover, our prior distributions were chosen to be plausible, but wide, in order to examine our model predictions over parameter space and are not suited for a robust statistical inference to select between which equilibrium tidal model best describes tidal interactions in low-mass binaries stars. Below, we offer observational tests that could discriminate between models.

4.6. *CPL or CTL?*

Accurate measurements of P_{rot} and e, especially out to long P_{orb}, can potentially discriminate between which equilibrium tidal model best describes tidal interactions in low-mass stellar binaries. Here, we outline three observational tests that can discriminate between the two models. The first test considers binaries with $P_{orb} < 10$ d that are likely tidally locked on eccentric orbits, but with $e < 0.23$. In this e regime, the CPL model predicts that the majority of systems are tidally locked into synchronous rotation and does not permit a supersynchronous rotation state, e.g. Eqn. (20). The CTL model, however, predicts a continuum of supersynchronous rotators on eccentric orbits, e.g. Eqn. (22). Supersynchronous rotation that is not due to tidal interactions can occur in extremely young, rapidly rotating systems that are still contracting along the pre-main se-
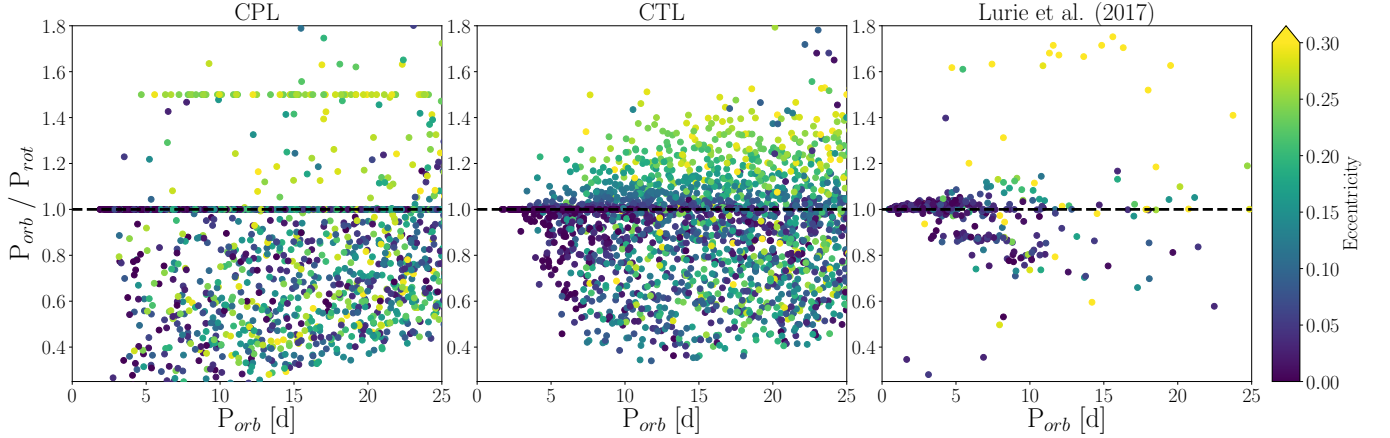
Figure 15. P_{orb}/P_{rot} as a function of P_{orb} according to the CPL model (left) and the CTL model (middle), and Lurie et al. (2017) *Kepler* EB observations (right). All points are colored by e. In the right panel, the *Kepler* EBs at low P_{orb} and low P_{orb}/P_{rot} are likely either brown dwarfs or exoplanets (Lurie et al. 2017), and hence are not modeled by our simulations, so we do not consider them, but we display them for completeness.

quence, or that have recently reached the main sequence. These young, supersynchronous rotators are unlikely to be tidally locked, usually have $P_{orb}/P_{rot} > 1.5$, and do not stay supersynchronous for long given that solar mass pre-main sequence lifetimes are $\lesssim 100$ Myr, distinguishing them from tidally locked binaries (see Fig. 15). If supersynchronous rotation is observed in binaries with $P_{orb} < 10$ d, $P_{orb}/P_{rot} < 1.5$, and $0 < e \lesssim 0.23$, it is evidence in favor of the CTL model over the CPL model.

Second, for tidally locked binaries with $e > 0.23$, the CPL model predicts supersynchronous rotation in the form of a 3:2 spin-orbit comensurability, e.g. the line at $P_{orb}/P_{rot} = 1.5$ seen in the left panel of Fig. 15, and no other spin state is permitted, compared to the continuum of supersynchronous rotation states in eccentric tidally locked rotators predicted by the CTL model. If a substantial clustering of stellar binaries with $P_{orb}/P_{rot} = 1.5$ is observed, it would be strong evidence in favor of the CPL model, but there is no obvious clustering of *Kepler* EBs near any spin-orbit resonance. These two tests can fail to discriminate between the CPL and CTL model, however, if the CPL model P_{eq} is a continuous function of e, e.g. Eqn. (21), as was argued by Goldreich (1966) and derived by Murray & Dermott (1999). In such a case, one would need a large number of accurate and precise measurements P_{orb} and e, with robust uncertainties, for tidally interacting binaries to discriminate between the CPL and CTL continuous P_{eq}, e.g. Eqn. (21) versus Eqn. (22). In practice, this is extremely observationally expensive as it requires extensive photometric and spectroscopic observations of many binaries.

A third test, the detection of tidally locked binaries with solar-mass primaries and $P_{rot} \gtrsim 60$ d, would pro-

vide strong evidence in favor of the CPL model as the CTL model cannot tidally lock stars beyond $P_{orb} \approx 60$ d, regardless of τ, e.g. Fig. 10. The CPL model, however, can tidally lock binaries out to $P_{orb} \gtrsim 90$ d. We recommend observers try to measure P_{rot} and e in binaries out to $P_{orb} = 100$ d to test this hypothesis, but we note that detecting P_{rot} for such slow rotators can be difficult due to small star spot modulation amplitudes (McQuillan et al. 2014; Lurie et al. 2017; Reinhold et al. 2018). Long term spectroscopic monitoring may be warranted in such cases.

5. DISCUSSION

In this work, we probed the long-term angular momentum evolution of low-mass stellar binaries, with a focus on P_{rot} in short and intermediate P_{orb} binaries. We considered the impact of two common equilibrium tidal models, magnetic braking, and stellar evolution. We performed a large suite of simulations for binaries with physically-motivated initial conditions out to $P_{orb} = 100$ and across a wide range of tidal dissipation parameters to examine the competition between tidal torques and magnetic braking for controlling the stellar P_{rot} evolution.

In our simulations, nearly all binaries with $P_{orb} \lesssim 4$ d have tidally-synchronized spins and circularized orbits, in good agreement with observations of *Kepler* EBs and binaries in the field. We showed for $P_{orb} \gtrsim 4$ d, primary stars in stellar binaries can rotate subsynchronously for Gyrs due to the competition between tidal torques and magnetic braking, or supersynchronously if they tidally lock on eccentric orbits. Our predictions are not strongly dependant on the choice of magnetic braking model, but rather are generic outcomes of the interaction between magnetic braking and tidal torques. Both the

CPL and CTL equilibrium tidal models predict that binaries tidally-interact at longer P_{orb} than have previously been considered, out to $P_{orb} \approx 60 - 100$ d. Many binaries with $P_{orb} \lesssim 20$ d tidally lock according to both models, in good agreement with previous results, but the CPL model predicts that binaries can readily tidally lock out to $P_{orb} \approx 100$ d. Tidal interactions can cause P_{rot} evolution in stellar binaries to differ from the long-term spin down due to magnetic braking experienced by single stars, decoupling P_{rot} from age. In tidally interacting binaries, gyrochronology, the technique of linking stellar P_{rot} to age, likely fails, potentially underestimating stellar ages by up to 300%. We caution that any application of gyrochronology methods to stars, especially those with $P_{rot} \lesssim 20$ d, should account for the possibility of stellar binarity to prevent deriving incorrect ages.

We compare the predictions of both the CPL and CTL models with observations of P_{rot} and P_{orb} of *Kepler* EBs by Lurie et al. (2017) and find that both can qualitatively reproduce many features seen in the data, validating our approach and suggesting that equilibrium tidal models can accurately model stellar-tidal evolution in low-mass stellar binaries. The lack of uncertainties on P_{rot}, the approximate orbital eccentricities derived by Lurie et al. (2017), and unconstrained completeness estimates prevent us from discriminating between which tidal model best describes tidal torques in low-mass binaries and from inferring tidal properties of low-mass stars given the *Kepler* EB data.

We described three observational tests that can distinguish between which equilibrium tidal model better describes tidal interactions in low-mass stellar binaries. We primarily suggest that observers measure stellar P_{rot} in binaries with solar-mass primaries for P_{orb} between $60 - 100$ d. If any tidally locked binaries are identified at long P_{orb}, this would be evidence in favor of the CPL model as we found that only binaries tidally interacting via the CPL model could tidally lock at such long P_{orb}. At shorter P_{orb}, precise measurements of P_{rot} and binary e and P_{orb} could distinguish between the CPL and CTL model in tidally locked systems, e.g. identifying if P_{eq} follows Eq. (20) vs. Eq. (22), especially if the CPL P_{eq} is in fact a discrete function of e. The observations required by these tests, however, are nontrivial. Beyond these tests, our model could be used to infer the tidal properties of binary stars, perhaps in a Markov Chain Monte Carlo framework, by directly comparing simulation results with the observed stellar

and orbital properties, given the observational uncertainties and reasonable prior probability distributions for parameters like the initial binary e. This analysis, however, is beyond the scope of this work and we leave it for future endeavors.

Our theoretical predictions outline a critical point: one cannot simply observe a short P_{orb} binary on a circular orbit and assume synchronization, nor can one observe a binary with $P_{orb} \gtrsim 20$ d and assume that tides have not impacted that system's angular momentum evolution. Stellar-tidal interactions can produce synchronous and subsynchronous rotation for short P_{orb} binaries on circular orbits, e.g. Fig. 4, depending on the age of the system, e.g. Fig. 8, and the strength of tidal dissipation, e.g. Fig. 6 and Fig. 7. Understanding the long-term angular momentum evolution of stellar binaries out to $P_{orb} = 100$ d requires detailed modeling of its coupled-stellar tidal evolution, and characterizing tidal dissipation parameters. Many new eclipsing stellar binaries will be discovered by TESS (e.g. Sullivan et al. 2015; Matson et al. 2018) and in analysis of K2 data. Obtaining precise orbital and rotational constraints for stellar binaries will permit detailed characterization of tidal interactions between low-mass stars and shed light into the long-term angular momentum evolution in stellar binaries.

Software: matplotlib: Hunter (2007), numpy: van der Walt et al. (2011), pandas: McKinney (2010), `VPLanet`: Barnes et al. (2019)

APPENDIX

A. ANALYTIC TORQUE BALANCE

Here we derive the equation for the stellar P_{rot} at which tidal torques balance magnetic braking discussed in § 4.1.1. As in § 4.1.1, we assume that both stars have $M = 1M_\odot$, 0 obliquity, and we assume a circular binary orbit. We assume that the torque balance occurs while the stars are on the main sequence, where stellar properties change slowly, so the angular momentum evolution is controlled by the balance between tidal torques and magnetic braking, not stellar radius contraction. Under this assumption, we can set $R = 1R_\odot$ and assume constant moments of inertia. For simplicity, we assume that magnetic braking proceeds under the Matt et al. (2015) model and the CTL model describes tidal torques.

As discussed in § 4.1.1, both stars are in the unsaturated rotation regime, so the torque due to magnetic braking is given by Eqn. (2), which under the aforementioned assumptions, reduces to

$$\left.\frac{dJ}{dt}\right|_{MB} = -C_{MB}\left(\frac{P_{rot,\odot}}{P_{rot}}\right)^3 \tag{A1}$$

where $P_{rot} = 2\pi/\omega$ and $C_{MB} = 6.3 \times 10^{30}$ ergs (Matt et al. 2015, 2019).

Under the CTL model and our assumptions, the change in rotation rate due to tidal torques, Eqn. 16, reduces to

$$\left.\frac{d\omega}{dt}\right|_{tides} = \frac{P_{orb}Z_{CTL}}{2\pi Mr_g^2R^2}\left(1 - \frac{P_{orb}}{P_{rot}}\right) \tag{A2}$$

where $P_{orb} = 2\pi/n$. For fixed moment of inertia, $dJ/dt = Id\omega/dt$, and after inserting Eqn. 18 for Z_{CTL}, the tidal torque on the stellar rotations becomes

$$\left.\frac{dJ}{dt}\right|_{tides} = \frac{C_{tides}k_2\tau}{P_{orb}^5}\left(1 - \frac{P_{orb}}{P_{rot}}\right). \tag{A3}$$

where $C_{tides} = 24\pi^5 R_\odot^5/G$.

The torques due to tides and magnetic braking balance when $\frac{dJ}{dt}|_{tides} + \frac{dJ}{dt}|_{MB} = 0$,

$$\frac{C_{tides}k_2\tau}{P_{orb}^5}\left(1 - \frac{P_{orb}}{P_{rot}}\right) - C_{MB}\left(\frac{P_{rot,\odot}}{P_{rot}}\right)^3 = 0. \tag{A4}$$

By specifying P_{orb} and $k_2\tau$, we can numerically solve Eqn. (A4) for the P_{rot} at which torques due to magnetic braking and tides balance, often producing subsynchronous rotation as seen in Fig. 3 and our simulations in § 4.1.

REFERENCES

Agüeros, M. A., Covey, K. R., Lemonias, J. J., et al. 2011, ApJ, 740, 110

Allain, S. 1998, A&A, 333, 629

Baraffe, I., Homeier, D., Allard, F., & Chabrier, G. 2015, A&A, 577, A42

Barker, A. J., & Ogilvie, G. I. 2009, MNRAS, 395, 2268

Barnes, R. 2017, ArXiv e-prints, arXiv:1708.02981

Barnes, R., Mullins, K., Goldblatt, C., et al. 2013, Astrobiology, 13, 225

Barnes, R., Luger, R., Deitrick, R., et al. 2019, arXiv e-prints, arXiv:1905.06367

Barnes, S. A. 2003, ApJ, 586, 464

—. 2007, ApJ, 669, 1167

—. 2010, ApJ, 722, 222

Bate, M. R. 2000, MNRAS, 314, 33

Bate, M. R., Bonnell, I. A., & Bromm, V. 2002, MNRAS, 336, 705

Bolmont, E., & Mathis, S. 2016, Celestial Mechanics and Dynamical Astronomy, 126, 275

Bonnell, I. A., & Bate, M. R. 1994, MNRAS, 271, astro-ph/9411081

Bouvier, J. 2008, A&A, 489, L53

Burkart, J., Quataert, E., & Arras, P. 2014, MNRAS, 443, 2957

Chaplin, W. J., Basu, S., Huber, D., et al. 2014, ApJS, 210, 1

Claret, A., Gimenez, A., & Cunha, N. C. S. 1995, A&A, 299, 724

Counselman, III, C. C. 1973, ApJ, 180, 307

Cranmer, S. R., & Saar, S. H. 2011, ApJ, 741, 54

Darwin, G. H. 1880, Philosophical Transactions of the Royal Society of London Series I, 171, 713

Douglas, S. T., Agüeros, M. A., Covey, K. R., & Kraus, A. 2017, ApJ, 842, 83

Duchêne, G., & Kraus, A. 2013, ARA&A, 51, 269

Fabrycky, D., & Tremaine, S. 2007, ApJ, 669, 1298

Ferraz-Mello, S., Rodríguez, A., & Hussmann, H. 2008, Celestial Mechanics and Dynamical Astronomy, 101, 171

Fleming, D. P., Barnes, R., Graham, D. E., Luger, R., & Quinn, T. R. 2018, ApJ, 858, 86

Fleming, D. P., & Quinn, T. R. 2017, MNRAS, 464, 3343

Gaia Collaboration, Prusti, T., de Bruijne, J. H. J., et al. 2016, A&A, 595, A1

Gallet, F., Bolmont, E., Mathis, S., Charbonnel, C., & Amard, L. 2017, A&A, 604, A112

Gallet, F., & Bouvier, J. 2013, A&A, 556, A36

—. 2015, A&A, 577, A98

Goldreich, P. 1966, AJ, 71, 1

Goldreich, P., & Peale, S. 1966, AJ, 71, 425

Goldreich, P., & Soter, S. 1966, Icarus, 5, 375

Greenberg, R. 2009, ApJL, 698, L42

Habets, G. M. H. J., & Zwaan, C. 1989, A&A, 211, 56

Haisch, Jr., K. E., Lada, E. A., & Lada, C. J. 2001, ApJL, 553, L153

Hamers, A. S., Perets, H. B., & Portegies Zwart, S. F. 2016, MNRAS, 455, 3180

Heller, R., Leconte, J., & Barnes, R. 2011, A&A, 528, A27

Herbst, W., Bailer-Jones, C. A. L., & Mundt, R. 2001, ApJL, 554, L197

Herbst, W., Bailer-Jones, C. A. L., Mundt, R., Meisenheimer, K., & Wackermann, R. 2002, A&A, 396, 513

Howell, S. B., Sobeck, C., Haas, M., et al. 2014, PASP, 126, 398

Hunter, J. D. 2007, Computing In Science & Engineering, 9, 90

Hurley, J. R., Tout, C. A., & Pols, O. R. 2002, MNRAS, 329, 897

Hut, P. 1981, A&A, 99, 126

Irwin, J., & Bouvier, J. 2009, in IAU Symposium, Vol. 258, The Ages of Stars, ed. E. E. Mamajek, D. R. Soderblom, & R. F. G. Wyse, 363–374

Ivanova, N., Belczynski, K., Fregeau, J. M., & Rasio, F. A. 2005, MNRAS, 358, 572

Jackson, B., Barnes, R., & Greenberg, R. 2009, ApJ, 698, 1357

Jackson, B., Greenberg, R., & Barnes, R. 2008, ApJ, 678, 1396

Keppens, R. 1997, A&A, 318, 275

Khaliullin, K. F., & Khaliullina, A. I. 2011, MNRAS, 411, 2804

Leconte, J., Chabrier, G., Baraffe, I., & Levrard, B. 2010, A&A, 516, A64

Levato, H. 1974, A&A, 35, 259

Lurie, J. C., Vyhmeister, K., Hawley, S. L., et al. 2017, AJ, 154, 250

MacGregor, K. B., & Brenner, M. 1991, ApJ, 376, 204

Mamajek, E. E., & Hillenbrand, L. A. 2008, ApJ, 687, 1264

Mardling, R. A., & Aarseth, S. J. 2001, MNRAS, 321, 398

Martin, D. V., Mazeh, T., & Fabrycky, D. C. 2015, MNRAS, 453, 3554

Mathis, S. 2015, A&A, 580, L3

Matson, R. A., Howell, S. B., & Ciardi, D. 2018, arXiv e-prints, arXiv:1811.02108

Matt, S. P., Brun, A. S., Baraffe, I., Bouvier, J., & Chabrier, G. 2015, ApJL, 799, L23

—. 2019, ApJL, 870, L27

Mazeh, T. 2008, in EAS Publications Series, Vol. 29, EAS Publications Series, ed. M.-J. Goupil & J.-P. Zahn, 1–65

McKinney, W. 2010, in Proceedings of the 9th Python in Science Conference, ed. S. van der Walt & J. Millman, 51 – 56

McQuillan, A., Mazeh, T., & Aigrain, S. 2014, ApJS, 211, 24

Meibom, S., Barnes, S. A., Platais, I., et al. 2015, Nature, 517, 589

Meibom, S., & Mathieu, R. D. 2005, ApJ, 620, 970

Meibom, S., Mathieu, R. D., & Stassun, K. G. 2006, ApJ, 653, 621

Mestel, L. 1968, MNRAS, 138, 359

Moe, M., & Kratter, K. M. 2018, ApJ, 854, 44

Muñoz, D. J., & Lai, D. 2015, Proceedings of the National Academy of Science, 112, 9264

Murray, C. D., & Dermott, S. F. 1999, Solar system dynamics

Ogilvie, G. I. 2013, MNRAS, 429, 613

Ogilvie, G. I., & Lin, D. N. C. 2007, ApJ, 661, 1180

Orosz, J. A., Welsh, W. F., Carter, J. A., et al. 2012, Science, 337, 1511

Raghavan, D., McAlister, H. A., Henry, T. J., et al. 2010, ApJS, 190, 1

Reiners, A., & Mohanty, S. 2012, ApJ, 746, 43

Reinhold, T., Bell, K. J., Kuszlewicz, J., Hekker, S., & Shapiro, A. I. 2018, arXiv e-prints, arXiv:1810.11250

Reinhold, T., Reiners, A., & Basri, G. 2013, A&A, 560, A4

Repetto, S., & Nelemans, G. 2014, MNRAS, 444, 542

Ricker, G. R., Winn, J. N., Vanderspek, R., et al. 2014, in Proc. SPIE, Vol. 9143, Space Telescopes and Instrumentation 2014: Optical, Infrared, and Millimeter Wave, 914320

Rodríguez, A., Callegari, N., Michtchenko, T. A., & Hussmann, H. 2012, MNRAS, 427, 2239

Rodríguez-Ledesma, M. V., Mundt, R., & Eislöffel, J. 2009, A&A, 502, 883

Simonian, G. V. A., Pinsonneault, M. H., & Terndrup, D. M. 2018, ArXiv e-prints, arXiv:1809.02141

Skumanich, A. 1972, ApJ, 171, 565

Stassun, K. G., Mathieu, R. D., Mazeh, T., & Vrba, F. J. 1999, AJ, 117, 2941

Sullivan, P. W., Winn, J. N., Berta-Thompson, Z. K., et al. 2015, ApJ, 809, 77

Tokovinin, A., Thomas, S., Sterzik, M., & Udry, S. 2006, A&A, 450, 681

Torres, G., Curtis, J. L., Vanderburg, A., Kraus, A. L., & Rizzuto, A. 2018, ApJ, 866, 67

van der Walt, S., Colbert, S. C., & Varoquaux, G. 2011, Computing in Science Engineering, 13, 22

Van Eylen, V., Winn, J. N., & Albrecht, S. 2016, ApJ, 824, 15

van Saders, J. L., Pinsonneault, M. H., & Barbieri, M. 2018, ArXiv e-prints, arXiv:1803.04971

Verbunt, F., & Zwaan, C. 1981, A&A, 100, L7

Witte, M. G., & Savonije, G. J. 2002, A&A, 386, 222

Zahn, J.-P. 1975, A&A, 41, 329

—. 1994, A&A, 288, 829

Zahn, J.-P. 2008, in EAS Publications Series, Vol. 29, EAS Publications Series, ed. M.-J. Goupil & J.-P. Zahn, 67–90

Zahn, J.-P., & Bouchet, L. 1989, A&A, 223, 112